Ground-based MAX-DOAS observations of tropospheric aerosols, NO$_2$, SO$_2$ and HCHO in Wuxi, China, from 2011 to 2014

Yang Wang[1], Johannes Lampel[1,2], Pinhua Xie[3,4,5], Steffen Beirle[1], Ang Li[3], Dexia Wu[3], and Thomas Wagner[1]

[1] Max Planck Institute for Chemistry, Mainz, Germany

[2] Institute of Environmental Physics, University of Heidelberg, Heidelberg, Germany

[3] Anhui Institute of Optics and Fine Mechanics, Key laboratory of Environmental Optics and Technology, Chinese Academy of Sciences, Hefei, China

[4] CAS Center for Excellence in Urban Atmospheric Environment, Institute of Urban Environment, Chinese Academy of Sciences, Xiamen, China

[5] School of Environmental Science and Optoeclectronic Technology, University of Science and Technology of China, Hefei, China

Correspondence to: Yang Wang (y.wang@mpic.de); Pinhua Xie (phxie@aiofm.ac.cn)

Abstract.

We characterize the temporal variation and vertical distribution of nitrogen dioxide (NO$_2$), sulphur dioxide (SO$_2$), formaldehyde (HCHO) and aerosol extinction based on long-term Multi Axis - Differential Optical Absorption Spectroscopy (MAX-DOAS) observations from May 2011 to November 2014 in Wuxi, China. A new inversion algorithm (PriAM) is implemented to retrieve profiles of the trace gases (TGs) and aerosol extinction (AE) from the UV spectra of scattered sunlight recorded by the MAX-DOAS instrument. We investigated two important aspects of the retrieval process. We found that the systematic seasonal variation of temperature and pressure (which is regularly observed in Wuxi) can lead to a systematic bias of the retrieved aerosol profiles (e.g. up to 20% for the AOD) if it is not explicitly considered. In this study we take this effect for the first time into account. We also investigated in detail the reason for the differences of tropospheric VCDs derived from either the geometric approximation or by the integration of the retrieved profiles, which were reported by earlier studies. We found that these differences are almost entirely caused by the limitations of the geometric approximation (especially for high aerosol loads). The results retrieved from the MAX-DOAS observations are compared with independent techniques not only under cloud free sky conditions, but also under various cloud scenarios. Under most cloudy conditions (except fog and optically thick clouds), the trace gas results still show good agreements. In contrast, for the aerosol results, only near-surface AE could be still well retrieved under cloudy situations.

After applying a quality control procedure, the MAX-DOAS data are used to characterize the seasonal, diurnal, and weekly variations of NO_2, SO_2, HCHO and aerosols. A regular seasonality of the three trace gases is found, but not for aerosols. Similar annual variations of the profiles of the trace gases appear in different years. Only NO_2 shows a significant seasonality of the diurnal variations. Considerable amplitudes of weekly cycles occur for NO_2 and SO_2, but not for HCHO and aerosols. The TGs and aerosols show good correlations, especially for HCHO in winter. More pronounced wind direction dependencies, especially for the near-surface concentrations, are found for the trace gases, than for the aerosols, which implies that the local emissions from nearby industrial areas (including traffic emissions) dominate the local pollution while long distance transport might also considerably contribute to the local aerosol levels.

1 Introduction

Nitrogen dioxide (NO_2), sulphur dioxide (SO_2), and formaldehyde (HCHO) are important atmospheric constituents which play crucial roles in tropospheric chemistry (Seinfeld and Pandis, 1998). NO_2 is involved in many chemical cycles such as the formation of tropospheric ozone. NO_2 and SO_2 can be converted to nitrate and sulphate, respectively, through the reaction with the OH radical. HCHO is formed mainly from the oxidation of volatile organic compounds (VOCs). Primary emissions of HCHO could be also important, especially in industrial regions (Chen et al., 2014). Due to the short life time of HCHO, it can be used as a measure of the level of the local VOC amount. The VOCs can then be eventually oxidized to form organic aerosols. NO_2, SO_2 and VOCs (marked by HCHO) are essential precursors of aerosols. During the industrialization and urbanization, anthropogenic emissions from traffic, heating, industry, and biomass burning have significantly increased the concentrations of these gases in the boundary layer in urban areas (Environmental Protection Agency, 1998; Seinfeld and Pandis, 1998). Nowadays, strong haze pollution events occur frequently around megacities and urban agglomerations, especially in newly industrializing countries like China, and have a significant impact on human health (Fu et al., 2014a). Recent studies found that in megacities in different regions of China most of aerosol particles are secondary, e.g. formed through photochemistry of precursor gases, during haze pollution events (Crippa et al., 2014 and Huang et al., 2014). Understanding the temporal variation and spatial distribution of trace gases (TGs) and aerosols through long-term observations is thus helpful to identify the dominating pollution sources, distinguish the contribution of transport and local emission as well as the relation between aerosols and their precursors. To accomplish this, a Multi Axis - Differential Optical Absorption Spectroscopy (MAX-DOAS) instrument was operated from 2011 to 2014 in Wuxi (China). Since about 15 years ago, the MAX-DOAS technique has drawn lots of attention because of the potential to retrieve the vertical distribution of TGs and aerosols in the troposphere from the scattered sunlight recorded at multiple elevation angles (Hönninger and Platt, 2002; Bobrowski et al., 2003; Van Roozendael et al., 2003; Hönninger et al., 2004; Wagner et al., 2004 and Wittrock et al., 2004) using relatively simple and cheap ground-based instrumentation. Ground-based measurements of TG profiles are complementary to global satellite observations and allow for inter-comparisons and validation exercises (Irie et al., 2008; Roscoe et al., 2010; Ma et al., 2013; Kanaya et al., 2014; Vlemmix et al., 2015a).

Using different inversion approaches, the column densities, vertical profiles and near-surface concentrations of the TGs and aerosols can be derived and provide additional information compared to in-situ monitoring or satellite observations.

The tropospheric vertical column density (VCD) of TGs is either derived by the geometric approximation (e.g. Brinksma et al., 2008) or by integration of the retrieved concentration profiles (Vlemmix et al., 2015b). The near-surface concentration can be derived using simplified rapid methods (Sinreich et al., 2013 and Wang et al., 2014b) or directly from the derived profile. The existing profile inversion schemes developed by different groups can be subdivided into two groups: the 'full profile inversion' based on optimal estimation (OE) theory (Rodgers, 2000; Frieß et al., 2006, 2011; Wittrock et al., 2006; Irie et al., 2008, 2011; Clémer et al., 2010; Yilmaz, 2012; Hartl and Wenig, 2013 and Wang et al., 2013a and b) and the so-called parameterization approach using look-up tables (Li et al., 2010, 2012; Vlemmix et al., 2010, 2011; Wagner et al., 2011). In comparison with the look-up table methods, the OE-based inversion algorithms are in principle easily applied to different species, different measurement locations and instruments, but they require radiative transfer simulations during the inversion and can therefore be computationally expensive for large datasets. Clémer et al. (2010), Frieß et al. (2011), Kanaya et al. (2014), Hendrick et al. (2014), Wang et al. (2014a) applied their OE approaches to long-term MAX-DOAS observations in different locations of the world. The stability and flexibility of the inversion algorithms depends on the choice of the inversion approach, the iteration scheme and the a-priori constraints (Vlemmix et al., 2015b). Here good stability means that an inversion approach is robust with respect to the effects of measurement noise. Good flexibility means that it can well retrieve diverse profile shapes. Designing an approach balancing stability and flexibility is quite important for long-term observations because of the occurrences of various atmospheric scenarios caused by natural variability and human activities.

In this study, we use the Levenberg-Marquardt modified Gauss-Newton numerical procedure (Yilmaz, 2012) with some modifications to optimally balance stability and flexibility, which will be referred to in the following as "**Pr**ofile **i**nversion algorithm of aerosol extinction and trace gas concentration developed by **A**nhui Institute of optics and fine mechanics, Chinese academy of sciences (AIOFM, CAS) in cooperation with **M**ax Planck Institute for Chemistry (MPIC)" (PriAM) (Wang et al., 2013a and b). The PriAM algorithm joined the intercomparison exercise of aerosol vertical profiles retrieved from MAX-DOAS observations, between five inversion algorithms during the Cabauw Intercomparison Campaign of Nitrogen Dioxide measuring Instruments (CINDI) in summer 2009 (Frieß et al., 2016). The intercomparison displayed good agreement of the aerosol extinction (AE) profiles, AODs and near-surface AEs retrieved by the PriAM algorithm with those by other algorithms and with a collocated ceilometer instrument, a sun photometer and a humidity-controlled nephelometer. In this work the PriAM is applied to the long-term MAX-DOAS observations in Wuxi, China. The retrieved results of NO_2, SO_2 and HCHO and aerosols are verified by comparisons with several independent data sets for a period longer than one year.

Under cloudy skies the retrieval algorithm could be subject to large errors because of the increased complexity of the atmospheric light paths inside clouds (e.g. Erle et al., 1995; Wagner et al., 1998, 2002, 2004; Winterrath et al., 1999), which are usually not considered in the forward model. Previous studies usually either ignored the effects of clouds or simply

discarded cloud-contaminated measurements. However, depending on location and season, a large fraction of measurements might be affected by clouds, e.g. about 80% of all MAX-DOAS measurements in Wuxi (Wang et al., 2015). We investigate the effect of clouds on the different MAX-DOAS retrieval results of aerosols and TGs, especially the near-surface concentrations by comparisons with results from independent techniques under various cloud scenarios. Information on different cloud scenarios is directly derived from the MAX-DOAS observations and can thus be assigned to each MAX-DOAS result without temporal interpolation. Tropospheric TG VCDs are also important for satellite validation. So far, most studies used the so-called geometric approximation to derive TG VCDs from MAX-DOAS measurements. However, considerable systematic discrepancies of tropospheric TG VCDs derived by the geometric approximation and by integration of the TG profiles are already reported in Hendrick et al. (2015), but which of the two values is closer to reality remains unclear. It is essential to answer this question in order to use a trustworthy method to determine the tropospheric TG VCDs. In this study we show evidence that the dominant error is associated with the geometric approximation, thus the TG VCDs by integration of the profiles are used for further studies here. After the series of verification exercises, the MAX-DOAS results are used to characterize temporal variations and vertical distributions of aerosols and TGs in Wuxi. The relation between aerosols and TGs are also discussed.

The paper is organized as follows: in section 2 the observations and different steps of the data analysis are described and results are verified. Moreover, the cloud effect on the retrievals and the errors of the geometric approximation are discussed. In section 3 we characterize seasonal variations and inter-annual trends, diurnal variations, weekly cycles and wind dependencies of the aerosols and TGs. The relation between aerosols and TGs are also discussed. In section 4 the results are summarized and conclusions are given.

2 MAX-DOAS measurements

2.1 MAX-DOAS in Wuxi

A MAX-DOAS instrument developed by AIOFM shown in Fig. 1a is located on the roof of a 11-story building in Wuxi City (Fig. 1b), China (31.57 °N, 120.31 °E, 50 m a.s.l.) at the transition between the urban and suburban area. The suburban area with lots of farmlands is located in the east, and Taihu Lake is located in the north. The heavily industrialised area and the urban centre (living and business area) are in southwest and northwest direction of the MAX-DOAS station, respectively. Wuxi city belongs to the Yangtze River delta industrial zone and is located about 130 km north-west of Shanghai (Fig. 1c). Wuxi is an important industrial city and has about six million inhabitants. Because of the high population density and high industrial activity, relatively high abundances of NO_2, SO_2 and VOCs are found (Fu, et al, 2013). Fig. 1d displays the mean distributions of NO_2 (Boersma et al., 2011), HCHO (de Smedt et al., 2010) and SO_2 (Theys et al., 2015) as derived from the Ozone Monitoring instrument (OMI) (Levelt et al., 2006 b). In north-west direction of Wuxi city the large industrial zone of North China plain is located, which has even higher pollution loads. The dominant wind is from the northeast and no

significant seasonality is observed (see Fig. S2 in the supplement). The meteorological conditions including, temperature, relative humility and wind field are introduced in section 1 of the supplement.

The MAX-DOAS instrument was operated by the Wuxi CAS Photonics Co. Ltd from May 2011 to December 2014. The instrument was pointed to the north and automatically recorded spectra of UV scattered sunlight at sequences consisting of

5   five elevation angles (5 °, 10 °, 20 °, 30 ° and 90 °). One elevation sequence scan took about 12 min depending on the received radiance. More details of the instrument can be found in Wang et al. (2015). During the whole observation period, the instrument stopped twice: 15 December 2012 to 29 February 2013 and 16 July to 12 August 2013.

2.2 Retrievals of the tropospheric profiles of aerosol extinction, NO_2, SO_2 and HCHO volume mixing ratios.

2.2.1 Retrieval of slant column densities

10   The slant column densities (SCDs) of the oxygen dimer (O_4), NO_2, SO_2 and HCHO are retrieved from scattered sunlight spectra measured by the MAX-DOAS instrument using the DOAS technique (Platt and Stutz, 2008) implemented by the WINDOAS software (Fayt and van Roozendael, 2009). SCD represents the TG concentrations integrated along the effective atmospheric light path. The TG cross sections, wavelength ranges and additional properties of the DOAS analyses are provided in Table 1. Figure 2 shows typical DOAS fit examples. We skip data for solar zenith angle (SZAs) larger than 75 °

15   because of stronger absorptions of stratospheric species and low signal to noise ratio. We also skip the data with large root mean square (RMS) of the residuals and large relative intensity offset (RIO). All thresholds of the quantities used for filtering the results and the percentages of screened data of the total number of observations are listed in Table 2. Detailed discussions of the DOAS fit parameters for each species can be found in section 2 of the supplement.

2.2.2 The PriAM algorithm

20   Tropospheric vertical profiles of AE and trace gases volume mixing ratios from the ground up to 4km are retrieved from the SCDs by using the PriAM algorithm, which was originally introduced by Wang et al. (2013a and b). Below we summarize the basic concept of the PriAM algorithm and its specific settings for this study, while details can be found in section 3 of the supplement. Like for other algorithms, a two-step inversion procedure is used in PriAM. In the first step, profiles of AE are retrieved from the O_4 dSCDs. Afterwards, profiles of NO_2, SO_2 and HCHO volume mixing ratios (VMRs) are retrieved from

25   the respective dSCDs in each MAX-DOAS elevation sequence. The retrieval problem is solved by the Levenberg-Marquardt modified Gauss-Newton numerical iteration procedure (Rodgers, 2000). Considering the frequent variation of aerosols and TGs, very little is known about the expected profiles. Thus a set of fixed a-priori profiles is used for each species. A smoothed box-shaped a-priori AE profile (Boltzmann distribution) (Yilmaz, 2012), exponential a-priori profiles of NO_2 and SO_2 (similar to Yilmaz, 2012 and Hendrick et al., 2014), and a Boltzmann distribution a-priori HCHO profile (based on the

30   MAX-DOAS and aircraft measurements in Milano during summer of 2003 reported in Wagner et al., 2011) are used in this

study and denoted by the black curves in Fig. S8 in the supplement. Besides these standard a-priori profiles, we tested the effect of changing the profile shapes and absolute values on the fit results. The description of these sensitivity tests is given in section 3.1 of the supplement. We conclude that the standard a-priori profiles are well suited for the application to the long-term MAX-DOAS measurements in Wuxi. We also find that improper a-priori profiles can strongly impact the aerosol

5   profile retrievals, but only slightly impact the TG results.

PriAM uses the radiative transfer model (RTM) SCIATRAN version 2.2 (Rozanov et al., 2005). Based on the wavelength intervals of the DOAS fits, the RTM simulations are done at 370 nm for the retrieval of aerosols and NO_2, at 339 nm for HCHO and at 313 nm for SO_2. The surface height and surface albedo are set as 50 m a.s.l. and 0.05, respectively. The fixed single scattering albedo of 0.9 and asymmetry factor (Henyey and Greenstein, 1941) of 0.72 are chosen according to average

10   inversion results from the Taihu AERONET station (see section 2.2.4) from 2011 to 2013 (the data in 2014 is unavailable). The retrieved AE at 370 nm is converted to those around 313 nm for the SO_2 and 339 nm for the HCHO retrieval using Ångström exponents derived also from the Taihu AERONET data sets.

In addition, here it should be noted that the Levenberg-Marquardt modified Gauss-Newton procedure is based on the assumption that the probability distribution function (PDF) of the atmospheric state (x) can be described by a Gaussian PDF

15   (P) around the a-priori state (x_a) (Rodgers, 2000):

$$-2 \ln P(x) = (x - x_a)^T S_a^{-1}(x - x_a) + c \qquad (1)$$

Here c is a constant value and S_a is the covariance matrix of the a-priori. Thus the solution can not reach the true state if the PDF of the atmospheric state (x) is skewed or asymmetric (Rodgers, 2000). In this study the retrieval of the AE for extremely high aerosol loads (e.g. fog and haze) belongs to cases, which probably do not fulfil this assumption. In such cases

20   the AE is underestimated by the inversion (see section 2.2.5).

The totally averaged averaging kernels (AKs) for retrievals of AE and the NO_2 VMRs for favourable measurement conditions, namely cloud-free sky with relatively low aerosol loading (the sky condition is directly identified by MAX-DDOAS observations as described in section 2.2.5), are shown in Fig. 5. AKs for SO_2 and HCHO are similar to those of NO_2. They indicate that the inversions are sensitive to the layers from the surface up to 1.5 km. The degrees of freedom (DoF) are

25   about 1.5 for aerosols (similar to Frieß et al., 2006), 2 for NO_2 and 2.3 for SO_2 and HCHO. The detailed discussion of the performance of the profile retrievals is given in section 3.2 of the supplement by comparing the measured and modelled dSCDs for different elevation angles, and comparing profiles, AKs and retrieval errors in different seasons. In general the retrievals performed consistently for different elevation angles and seasons.

2.2.3 Correcting the effect of the variation of ambient temperature and pressure

30   In previous studies (Clémer et al., 2010; Hendrick et al., 2014; Wang et al. 2014a) usually fixed temperature and pressure (TP) profiles are used (e.g. obtained from the US standard summer atmosphere for the measurements in China). However for locations with a significant and systematic annual variation of TP, as in this study, this simplification can affect the retrieved

AODs and AE profiles (and thus also the TG profiles) systematically, yielding virtual seasonal variations. The time series of TP near the surface from the weather station near the MAX-DOAS instrument are shown in Fig. 3 for the year 2012 (similar patterns are found for other years, see Fig. S16 in the supplement). A regular annual variation of surface TP is obvious with amplitudes between winter and summer of about 20 K and 30 hPa, respectively. The O_4 VCDs derived from the fitted curves of surface TP (the method is described in section 3.3 of the supplement) is also shown in Fig. 3. The O_4 VCD in summer is systematically lower than in winter by about 15% of the yearly mean O_4 VCD. Ignoring this systematic seasonal variation can cause a 20-30% bias of the AOD and near-surface AE (see Fig. S17 of the supplement). The error of the aerosol retrieval can further nonlinearly impact the TG profile retrievals. To account for this effect, the seasonal variation of TP and the O_4 VCD is parameterized and explicitly considered in the forward model during the MAX-DOAS retrievals by the PriAM algorithm. Figure 4 shows the AODs retrieved by PriAM using either explicit TP information or the TP profiles from the US summer standard atmosphere. The consistency of the AODs retrieved based on the explicit TP data with the simultaneous Taihu AERONET level 1.5 AOD data sets (see section 2.2.4) is better than for TP profiles from the US standard summer atmosphere.

The systematic variation of TP could be also considerable in many other locations of the world. A seasonal variation of temperature occurs in many locations, especially outside the tropics. However the temporal variation of the pressure is usually more complex and strongly depends on the location. The variation of pressure in Wuxi (and also many other parts of Eastern China) is related to the East Asian Monsoon and shows a systematic seasonal pattern. The monsoon is a general phenomenon in Eastern China. The pressure over the continent is systematically lower and higher than that over the ocean in summer and winter, respectively. Thus a similar seasonal variation of the O_4 VCD is expected in general in Eastern China.

2.2.4 Comparisons with independent data sets under clear skies

To validate the results from MAX-DOAS observations, the column densities and averaged concentrations in the lowest layer from 0 to 200m are compared to independent measurements:

(a) AODs at 380 nm (level 1.5) from the sun photometer at the AERONET (Holben et al., 1998 and 2001) Taihu station. The data is downloaded from the website of http://aeronet.gsfc.nasa.gov/. The AERONET sun photometer is located 18 km south west of the MAX-DOAS instrument. AERONET data in the period from May 2011 to October 2013 is included in the study. In the level 1.5 data, a cloud screening scheme is used to filter most of the cloud contaminated data (Smirnov et al., 2000). Here it should be noted that AERONET Taihu station is located in a more remote area in Wuxi city than the MAX-DOAS instrument. This could contribute to a systematic bias between both data sets. However the long residence time of up to several days (Ahmed et al., 2004) and the relatively homogeneous horizontal distribution of aerosols (illustrated by the weak dependence of AOD on wind direction, see section 3.4.2) implies that the differences between both measurements should be small.

(b) Visibilities near the ground from a forward-scattering visibility meter (Manufacturer: Anhui Landun Photoelectron Co. Ltd. Model: DNQ2 forward-scattering visibility meter) (Wang et al., 2015), which is located at the same site as the MAX-DOAS instrument. The data from May 2011 to December 2013 is available.

(c) NO_2 and SO_2 VMRs (no HCHO data are available) near the ground from a long path DOAS (LP-DOAS) instrument (Qin et al., 2006) located at the same site as the MAX-DOAS instrument. The LP-DOAS is directed to the East with a total light path length of about 2km. The data from May 2011 to April 2012 is available

MAX-DOAS results are compared to the available independent measurements within 15 minute time difference. In this section only the data recorded during clear sky conditions with low aerosol load (the sky condition is identified by MAX-DOAS observations as described in section 2.2.5) are compared (comparisons for different cloud conditions are shown in section 2.2.5). For the comparisons of AODs, near-surface AE, NO_2 and SO_2 VMRs, the averaged absolute differences, standard deviations, correlation coefficients (R) (Pearson's product moment correlation coefficient is applied in this paper) and the slopes and intercepts derived from the linear regressions are shown in Fig. 6 for the different seasons. The histograms of the absolute differences in different seasons are shown in Fig. S18 in the supplement.

For the comparisons of AODs from MAX-DOAS and AERONET sun photometer, almost symmetrical Gaussian-shape histograms of the absolute difference are found for different seasons except summer (see Fig. S18a in the supplement). The mean differences of AODs are smaller than 0.16 (about 20% of the average value). The correlation coefficients are within 0.56 to 0.91 (see Fig 6). The highest R of 0.91 is found in summer, probably related to the wider range of AODs covered, but in that season also the largest absolute difference of -0.16 is found probably due to the stronger aerosol load than in other seasons. Underestimation of high aerosol amounts by MAX-DOAS will be discussed in section 2.2.5. Several previous studies applied a correction factor to measured O_4 dSCDs to improve the consistency between the AODs derived from MAX-DOAS and those from AERONET (e.g. Wagner et al., 2009; Clémer et al., 2010 and Frieß et al., 2016). So far there is no good explanation for this correction factor. In this study we don't apply any correction factor, because we achieve reasonable consistency between MAX-DOAS and AERONET results without the application of a correction factor.

The averaged AE in the lowest layer derived from the MAX-DOAS are compared with those from the visibility meter. Here it has to be noted that both instruments do not probe exactly the same air masses: the visibility meter is sensitive to air masses at the measurement location while the MAX-DOAS is sensitive to the air masses along the line of sight for up to several kilometres away from the instrument and up to a few hundred meters above the ground. Figure S18b in the supplement shows almost symmetrical Gaussian-shape histograms of the absolute differences of the AE between the two techniques. The mean differences are < 0.18 km^{-1} (about 33% of the average value) as shown in Fig. 6. The highest R of 0.74 is found in summer (see Fig. 6) probably related to the wider range of values and the stronger vertical convection, which causes a higher boundary layer and possibly a smoother vertical distribution of aerosols than in other seasons. The worst correlation is found in spring, which might be related to the occurrence of long-distance transport of dust with elevated aerosol layers (see section 3.1).

The VMRs of NO_2 and SO_2 in the lowest layer derived from MAX-DOAS are compared with the values from LP-DOAS measurements for the individual seasons. Like for the AE, it has to be noted that both instruments do not probe exactly the same air masses; as the LP-DOAS yields the mean TG concentration for the light path defined by the set-up of instrument and reflector. In general the mean absolute differences are smaller than 5 ppb (about 50% of the average value) for NO_2 and 6 ppb (about 60 % of the average value) for SO_2 (see Fig. 6). Almost symmetrical Gaussian-shape histograms of the absolute differences are also found for NO_2 and SO_2 in different seasons (Fig. S18c and d in the supplement). The range of R is from 0.4 to 0.7 for NO_2 and from 0.7 to 0.8 for SO_2 in all seasons (see Fig. 6). The higher R value for SO_2 than for NO_2 is probably related to the longer lifetime and thus more homogeneous vertical and horizontal distribution of SO_2 compared to NO_2, especially in the layer from 0 to 200m. The worst correlation of NO_2, especially in the afternoon (see Fig. S19 in the supplement) is found in summer probably because of the low NO_2 VMR near the surface, the small value range and the steep vertical gradient in the layer from 0 to 200m (see below). The generally positive absolute differences of NO_2 and SO_2 shown in Fig. 6 could be attributed to strong gradients in the layer from 0 to 200m as e.g. found from tower measurements in Beijing, Meng et al. (2008): they concluded that the largest values of the NO_2 and SO_2 concentrations are not directly located at the surface, but at an altitude of about 100 meters, especially in summer. However, it should be noted that the vertical gradients around Wuxi might be different from those in Beijing and thus also other reasons might contribute to the observed differences.

2.2.5 Evaluations of retrievals under cloudy and strong aerosol conditions.

The retrieval of AE by PriAM from O_4 absorptions is based on a RTM, which does not include the effects of clouds. In principle it should be possible to also include cloud effects in the RTM (at least for horizontally homogenous clouds), but in the current version of our retrieval this is not yet accomplished. In this section, we investigate how strongly different types of clouds affect the MAX-DOAS retrieval results of aerosols and TGs. For that purpose we compare the MAX-DOAS results with independent data sets for different cloud types. For the characterization of the cloud conditions we use the cloud classification scheme described in Wang et al., 2015 (based on the concept of Wagner et al., 2014) to classify the sky conditions from the MAX-DOAS observations, i.e. radiance, colour index and O_4 absorption. The scheme differentiates between eight primary sky conditions (varying between clear skies with low aerosol load to continuous cloud cover) and two secondary sky conditions of fog and optically thick clouds. In this study we condense the eight primary sky conditions to five primary conditions by merging two types of cloud holes and two types of continuous clouds and ignoring the rare condition of "extremely high midday CI" (Wang et al., 2015). The remaining five primary conditions are clear sky with low aerosol load ("low aerosol"), clear sky with high aerosol load ("high aerosol"), "cloud holes", "broken clouds", and "continuous clouds". Please note that "low" and "high" in the marks of sky condition categories describe the aerosol load but not the aerosol height. Each MAX-DOAS measurement scan is assigned to one of the five primary sky conditions. In addition, they can be assigned to the two secondary sky conditions of "fog" and "optically thick clouds". Here it should be

clarified that the "fog" sky condition does not exactly belong to the meteorological definition, but represents a sky condition derived from MAX-DOAS observations with a low visibility. It should be also noted that the distinction between "low aerosol" and "high aerosol" conditions is based on the colour index measured by the MAX-DOAS instrument, but not on explicit AOD threshold values. The studies of Wang et al., 2015, however, demonstrated that the AODs observed by the Taihu AERONET sun photometer are mostly smaller and larger than 0.6 for the "low aerosol" and "high aerosol", respectively. In addition to the cloud effect, also the effect of high aerosol loads is evaluated (due to the unrealistic assumption of the pdf of the atmospheric state in the OE algorithm for high aerosol loads (see Eq. (1)).

Firstly measured and modelled dSCDs (results of the forward model) are compared under various sky conditions. In Fig. 7 (grey columns), the histograms of the differences between the measured and modelled dSCDs are shown for the four species (note Figure 7 represents the differences for all non-zenith elevation angles). The histograms are symmetric and the maximum probabilities occur around zero for all four species. i.e., overall, there is no indication for a significant systematic retrieval bias. In the same figure, the relative frequencies for the different sky conditions are shown in different colours. In general, for cloudy sky conditions, especially for continuous clouds and optically thick clouds, larger discrepancies are found compared to cloud free sky conditions. The effect of clouds on the inversion is stronger for aerosols than for TGs. For the aerosol inversion, more negative differences are found for "fog", which indicates that the strong extinction in "fog" is not well represented by the forward model (The phenomenon is also found in Fig. 9 and discussed below). To skip those inverted profiles, which probably differ largely from the real profiles, we only keep the profiles, for which the differences between measured and modelled dSCDs are smaller than 2×10^{42} molecules^2 cm^{-5} for the O$_4$ dSCDs (90.6% of the total observations) and 5×10^{15} molecules cm^{-2} for NO$_2$ (89.8%), SO$_2$ (90.4%), and HCHO dSCDs (97.9%) for each elevation angle in one elevation sequence.

After this screening of potentially bad profiles, the mean profiles of AE and TG mixing ratios as well as the corresponding total AKs (which represent the sum of all AKs at the individual altitudes) are shown in Fig. 8 for different sky conditions. While the total AKs differ only slightly, the resulting profiles are quite different for different sky conditions. There are two interesting findings for the retrieved profiles: first, for all cloudy scenarios (incl. fog), the maximum AE is not found at the surface, but at higher altitudes, as observed also by Nasse et al., (2015). This can be explained by the fact that clouds act as a diffusing screen. The effect on MAX-DOAS observations is that the light paths, especially for low elevation angles, become longer than for cloud-free conditions. Consequently, also increased O$_4$ absorptions are measured for such conditions. A similar effect can also be caused by elevated aerosol layers. Since the forward model does not explicitly include clouds, usually elevated 'cloud-induced' aerosol layers are derived in the profile inversion under cloudy conditions. The diffusing screen effect depends on the cloud optical thickness. The most pronounced cloud-induced elevated aerosol layers are retrieved for optically thick clouds.

Interestingly, also for measurements under "fog" conditions, elevated aerosol layers are obtained from the MAX-DOAS inversion. This is at first sight surprising, but can be explained by two aspects: first, for most measurements classified as "fog", still a weak systematic dependence of the O$_4$ dSCDs on elevation angles is found, indicating that during most "fog"

events the visibility is still not close to zero. Second, for most of the measurements classified as "fog" also the presence of clouds (including thick and broken clouds) was detected (Wang et al., 2015). This finding indicates that, for most observations classified as "fog", increased aerosol scattering close to the surface occurred indeed, but at higher altitudes, even larger extinction was present. We also found a generally larger value of the cost function under cloudy conditions (consistent with Fig. 7) and a systematic variation of the TG VCDs and near-surface VMRs for the different cloud scenarios. Besides measurement errors, these variations are probably also due to different photolysis rates and atmospheric dynamics (see Fig. S20 in the supplement).

In the following we compare the results from MAX-DOAS and other techniques under different sky conditions. Since the frequencies of different cloud conditions depend on season (Wang et al., 2015) and also the agreement between MAX-DOAS and other techniques was found to be different for different seasons (see section 2.2.4), the comparisons are done for individual seasons. In Fig. 9 the comparison results in autumn are shown (similar conclusion are found for other seasons and the relevant figures are shown in Fig. S21 – S24 in the supplement). Based on the comparisons of the retrieved profiles under different sky conditions (Fig. 8) and the comparison results with independent data sets (Fig. 9), we have developed recommendations, under which sky conditions which data product might be still useful or should better not be used. These recommendations, as summarized in Table 3, should not be seen as binding, but rather as a general indication of the usefulness of a given observation, and might change for improved inversion algorithms in the future.

In general we find that the aerosol results are more strongly affected by the presence of clouds than the trace gas results. This is especially true for the retrieved AOD for which large mean difference and worse correlation are found under "continuous clouds" (see Fig. 9). The impact of clouds on the retrieved AE profiles is also significant, as illustrated in Fig. 8a. Thus we recommend that retrieved AOD and AE profiles (except close to the surface) should not be used for cloudy conditions. However, AE close to the surface can still well be retrieved under most cloudy conditions, except for "thick clouds" and especially for "fog", because a significant increase of the mean difference and decrease of the linear correlation are found for "fog" (Fig. 9). The TG results are less affected by clouds. No significant effects of clouds on the profiles of TGs are found, as can be seen in Figs. 8c, e, and g. Only larger mean differences and worse linear correlations of the surface mixing ratios are obtained for "thick clouds" and "fog" (Fig. 9). Thus not only surface mixing ratios, but also TG profiles and tropospheric VCDs can still be well retrieved for most cloudy situations (except for thick clouds and fog). The MAX-DOAS data used in Section 3 are filtered by the recommendations listed in Table 3.

In comparison with other sky conditions except "fog" and "thick clouds", outlier values of the mean differences and slopes under "high aerosol" conditions are found for both aerosols and TGs, as shown in Fig. 9. This phenomenon could attribute to two factors: a degraded performance of aerosol profile retrieval and a reality of vertical distributions of aerosols and TGs. On the one hand, aerosol profiles with high aerosol loadings could be hardly well reproduced by the retrieval algorithm due to the constraint of the a-priori profile and the assumption of Eq. (1). This is indicated by the systematic overestimation of the modelled O_4 dSCDs compared to the measured O_4 dSCDs as shown in Fig. 7 for "high aerosol" conditions. On the other hand, a "high aerosol" condition usually indicates a polluted period, therefore it is reasonable to expect a very different

inhomogeneity of the horizontal and vertical distributions of aerosols and TGs in the lowest layer (0-200m) of MAX-DOAS profile retrievals compared to other relative clean conditions. Thus different air mass observed by a MAX-DOAS instrument and other techniques could play a different role under "high aerosol" conditions. Further studies on the evaluation and improvement of profile retrievals of MAX-DOAS under heavy aerosol pollution conditions need to be carried out in the future. In this study, we decide to keep the MAXDOAS retrievals under "high aerosol" condition because, despite of their lower reliability, they can still provide useful information.

2.2.6 Error budgets

For the MAX-DOAS results, we derive the error estimates from different sources. First we estimate the error budgets for the near surface values and column densities of the TGs and aerosols, which are summarized in Table 4. The following error sources are considered:

(a) Smoothing and noise errors (fitting error of DOAS fits) on the near-surface values and column densities are derived from the averaged error of profiles from the retrievals (shown in Fig. S11b - S14b in the supplement), and amount on average to 10% and 6% for aerosols, 12% and 17% for NO_2, 19% and 25% for SO_2 and 50% and 50% for HCHO, respectively.

(b) Algorithm errors related to an imperfect minimum of the cost function, namely the discrepancy between the measured and modelled dSCDs. Based on the fact that measurements for 5 ° and 30 ° elevation angles are sensitive to low and high air layers, respectively, we estimate the algorithm errors on the near-surface values and the column densities using the averaged relative differences between measured and modelled dSCDs for 5 ° and 30 ° elevation angle, respectively. These errors on the near-surface values and the column densities are on average estimated at 4% and 8% for aerosols, 3% and 11% for NO_2, 4% and 10% for SO_2, 4% and 11% for HCHO, respectively.

(c) Cross section errors of O_4 (aerosols), NO_2, SO_2, and HCHO are 5%, 3%, 5% and 9%, respectively according to Thalman and Volkamer (2013), Vandaele et al. (1998), Bogumil et al. (2003) and Meller and Moortgat (2000).

(d) The errors related to the temperature dependence of the cross sections are estimated in the following way. We first calculate the amplitude changes of the cross sections per kelvin using two cross sections at two temperatures from the same data sets. Then the amplitude changes per kelvin are multiplied by the variation magnitude of the ambient temperature (45 K during the whole measurement period, see Fig. 3). The corresponding systematic error of O_4 (aerosols), NO_2, SO_2 and HCHO are estimated to up to 10%, 2%, 3% and 6%, respectively.

(e) The errors of TGs related to the errors of aerosols are estimated at 16% for VCDs and 15% for near-surface VMRs for the three TGs according to the total error budgets of aerosol retrievals. These estimations are based on a linear propagation of the aerosols errors on the TG retrievals, which is a rough assumption. Additional sensitivity tests considering uncertainties on aerosol properties and profiles should be performed for the different viewing geometries in order to derive a more realistic error estimate.

The total error budgets on the TGs and aerosols are given by combining all the above error sources in the bottom row of Table 4. In general the sum of the smoothing and noise error is the dominant error source in the total error budget. The error budgets of the profiles also consist of the five (four for aerosol profiles) error sources. The error (a) depends on the height, has much larger (relative) error at high altitudes and is shown in Fig. S11b - S14b in the supplement. The error (b) can not be realistically estimated because of the difficulty of assigning discrepancies between measured and modelled dSCDs to each altitude of profiles. The error (c) and (d) have identical values at all altitudes and are the same as the estimations for the near surface values and column densities above. The error (e) of TG profiles can be estimated as the total error budgets of aerosol profiles. However because of error (b) is unknown, the error (e) can not be quantified at the moment.

2.3 Comparisons between the geometric VCD and the VCD derived from the profile inversion

The geometric approximation (e.g. Brinksma et al., 2008) is often used to convert the dSCD for an elevation angle of α ($dSCD_\alpha$) to the tropospheric VCD_{geo} as Eq. (2):

$$VCD_{geo} = \frac{dSCD_\alpha}{\frac{1}{sin(\alpha)} - 1} \tag{2}$$

Elevation angles between about $20°$ and $30°$ are usually used for the application of the geometric approximation (e.g., Shaiganfar et al., 2011 and Ma et al., 2013). The tropospheric VCD (VCD_{pro}) can also be derived by the vertical integration of the retrieved profiles. The relative differences ($Diff_{total}$) between VCD_{pro} and VCD_{geo} for NO_2, SO_2 and HCHO are calculated by Eq. (3):

$$Diff_{total} = \frac{VCD_{geo} - VCD_{pro}}{VCD_{pro}} \tag{3}$$

In Fig. 10, the average relative differences for elevation angles of $20°$ and $30°$ are shown as function of the relative azimuth angle (RAA), i.e. the difference between the azimuth angles of the sun and the viewing direction of the telescope. In general, the discrepancy is larger for an elevation angle of $30°$ than for $20°$. In addition, also an increase of the difference with increasing relative azimuth angle is found. Both findings have different magnitudes for the different TGs. The observed dependencies could be attributed to two reasons: first, the validity of the geometric approximation is limited, especially if the last scattering event occurs in the TG layer of interest. The respective probability depends on the layer height, wavelength, aerosol load and viewing geometry. A second reason for the observed differences is the uncertainty of the profile inversion. Some studies already reported systematic errors of the geometric approximation:

1) Ma et al. (2013) showed that the systematic error of the NO_2 VCDs calculated by the geometric approximation for an elevation angle of $30°$ is about 20% on average, which is quite similar with the values shown in Fig. 10b. Also, the error is larger for larger elevation angles and larger RAA, which is also consistent with the results shown in Fig. 10a and b.

2) The simulation studies for an elevation angle of $22°$ in Shaiganfar et al. (2011) show that the error of the geometric approximation depends on the layer height of the TGs and aerosols. They found that a higher layer of TGs leads to a

larger negative error. This finding is consistent with the results shown in Fig 10e, where the largest biases are found for HCHO, which has a higher layer height than NO_2 and SO_2 (see Fig. 13)

To identify the dominant error source, we split the total difference ($Diff_{total}$) between VCD_{geo} and VCD_{pro} into two parts: The first part is the difference between VCD_{geo} and VCD_{geo}^m. Here VCD_{geo}^m is calculated by applying the geometric approximation to the modelled dSCD (from the forward model of the profile inversion) for the same elevation angle. This difference describes the error from the profile inversion and is referred to as $Diff_{inversion}$:

$$Diff_{inversion} = \frac{VCD_{geo} - VCD_{geo}^m}{VCD_{pro}}$$ (4)

The second part is the difference ($Diff_{geometry}$) between VCD_{geo}^m and VCD_{pro}:

$$Diff_{geometry} = \frac{VCD_{geo}^m - VCD_{pro}}{VCD_{pro}}$$ (5)

$Diff_{geometry}$ describes the error due to the limitation of the geometric approximation. $Diff_{inversion}$ and $Diff_{geometry}$ are also shown in Fig. 10 with red and blue colours, respectively. It is found that $Diff_{inversion}$ is mostly smaller than 4% for the 30 ° elevation angle of and smaller than 2% for the 20 ° elevation angle. Moreover, the variation of $Diff_{total}$ along RAA is similar with $Diff_{geometry}$. Both findings clearly indicate that the error due to the limitation of the geometric approximation is the dominant error contributing to $Diff_{total}$. Moreover the systematic errors of the geometric approximation become significant when the aerosol load is large (see section 4 of the supplement). Thus in the following, we integrate the retrieved profiles to extract the respective tropospheric VCD. One point needs to be clarified that the discrepancy of retrieved profile from the reality doesn't impact $Diff_{geometry}$, although both VCD_{pro} and VCD_{geo}^m for the calculation of $Diff_{geometry}$ are as function of the retrieved profile. Meanwhile $Diff_{inversion}$ can well present the discrepancy.

3 Results and discussion

In this section, MAX-DOAS results of column densities, near-surface concentrations and vertical profiles of aerosols and TGs are shown and discussed for a) seasonal variations and inter-annual trends, b) diurnal variations, c) weekly cycles as well as wind dependencies.

3.1 Seasonal variations and inter-annual trends of daytime NO₂, SO₂, HCHO and aerosols

The time series of monthly averaged (after daily averaging) TG VCDs and near-surface VMRs as well as AODs and near-surface AE (all the data are filtered by the recommended scheme in Table 3) derived from MAX-DOAS observations are presented in Fig. 11. Also shown are AODs and AE obtained from AERONET and visibility meter, respectively.

Similar annual variations are found for TG VCDs and near-surface VMRs. The seasonal cycles of NO_2 and SO_2 show minimum values (NO_2 and SO_2 VCD of 9-17×10¹⁵ and 12-23 ×10¹⁵ molecules cm⁻², respectively; NO_2 and SO_2 VMR of 5-

11 and 4-11 ppb, respectively) in summer and maximum values (NO$_2$ and SO$_2$ VCD of 27-35$\times$10^{15} and 33-54 $\times$10^{15} molecules cm^{-2}, respectively; NO$_2$ and SO$_2$ VMR of 12-16 ppb and 14-18 ppb) in winter. These characteristics are already well-known over urban areas in the eastern China region (Richter et al., 2005; Qi et al., 2012; Ma et al., 2013; Hendrick et al., 2014 and Wang et al., 2014a). In contrast, HCHO shows an opposite seasonality compared to NO$_2$ and SO$_2$. The HCHO VCD and near-surface VMR are 16-20$\times$10^{15} molecules cm^{-2} and 4-6 ppb in summer, respectively, 7-10$\times$10^{15} molecules cm^{-2} and 2-4 ppb in winter, respectively. A similar seasonality of HCHO in the eastern China region was already reported by De Smedt et al. (2010 and 2015).

For AOD and AE no pronounced seasonal cycle is found. The MAX-DOAS results mostly reveal similar levels like the other two techniques. Note that the data in 2014 is neither available from the AERONET Taihu station nor from the visibility meter. The AOD is typically larger than 0.7 and the AE typically larger than 0.5 km^{-1}. Note that the extremely low values in July and August of 2013 are unrepresentative because of poor statistics caused by the temporal shutdown of the instrument (see Fig. 11c).

The observed seasonal variations of the different species are related to various processes: the seasonal variation of source emissions, chemical (trans-) formation and destruction, dry and wet deposition, and atmospheric transport (Wang et al., 2010; Lin et al., 2011). Different from the column densities, the near-surface concentrations of all species can be systematically affected by the seasonality of the boundary layer (BL) height (Baars et al., 2008). The compression effect of the lower BL height in winter than in summer systematically increases the near-surface concentrations.

The details for the different species are discussed as follows:

1) NO$_2$ and SO$_2$

NO$_2$ (rapidly formed from NO$_x$ after its emission) and SO$_2$ originate mostly from direct emissions. It is assumed that about 94% of total NO$_x$ emission in the Wuxi region are from power plants, industrial fuel combustion, and vehicles (Huang et al., 2011), which emit similar amounts in different seasons. The contribution of boilers for the seasonal use of domestic heating to NOx is only about 5% (Huang et al., 2011). Thus the seasonal variation of the MAX-DOAS results cannot be explained by the variation of the NO$_x$ emissions. However, the SO$_2$ emissions might vary by about 20% due to the significant contribution of boilers (Huang et al., 2011). Because of the short lifetime of NO$_x$ under urban pollution (usually a few hours, e.g. Beirle et al., 2011 and Liu et al., 2015), most NO$_x$ should originate from local emissions (Liu et al., 2015), and NO$_x$ long-range transport could be negligible in Wuxi. It needs to be noted that because of the longer life time of NO$_x$ in winter (Schaub et al., 2015) than in summer, transport of NO$_2$ from a nearby pollution area in winter might play a role on the seasonality of NO$_2$. Due to the large range of SO$_2$ residence time (from less than one hour to 2 weeks and longer in winter than in summer, e.g. von Glasow et al., 2009; Lee et al., 2011; Beirle et al., 2014), transport from the highly polluted regions in the east and north likely plays a role, especially in winter. Here it is interesting to note that indications for long range transport of SO$_2$ are also found in the elevated SO$_2$ profiles in winter as shown in Fig 13b. Because of the strong seasonal variation of the SO$_2$ emissions due to domestic heating in the North (Wang et al., 2014a), long range transport from these regions could strongly impact the SO$_2$ amount in Wuxi in winter, thus contributing to the seasonality. In conclusion, the

seasonality of NO_2 can be mostly attributed to the removal mechanisms due to the OH radical, which has a minimum in winter and maximum in summer (Stavrakou et al., 2013). The same removal mechanism could be partly responsible for SO_2 seasonality (Lee et al., 2011). Additional heterogeneous reactions (Oppenheimer et al., 1998) might also play a role. Since we find a high correlation between the NO_2 and SO_2 VCDs and near surface VMRs (see Fig. S26 in the supplement), we conclude that also for SO_2 the seasonality of the removal mechanism is the most important factor controlling the seasonality of the SO_2 VCDs and near-surface VMRs.

2) HCHO

HCHO originates mainly from the oxidation degradation of many VOCs by the OH radical. But because the OH radical also plays a role in the removal mechanism of HCHO, the seasonal variation of the OH radical level contributes to the seasonality of HCHO in a complex way. Apart from the ubiquitous background levels of HCHO from the methane oxidation, emissions of non-methane VOCs (NMVOCs) (including HCHO) from biogenic sources, biomass burning and anthropogenic sources control local HCHO concentrations. Therefore, in addition to the seasonality of OH, also the seasonal variations of the VOC emissions should be important factors for the HCHO seasonality. Firstly stronger biogenic emissions are expected in the growing period, namely from spring to autumn. Based on a study in Beijing (Xie et al., 2008) a relative contribution of biogenic emissions to the total VOC levels is estimated at about 13%. Secondly, biomass burning events frequently occur in May and June (Cheng et al., 2014) in the Wuxi region. Thirdly anthropogenic emissions contribute a lot to the VOCs amounts. However the dominating sources, such as non-combustion industrial processes and vehicles (Huang et al., 2011), do not show an obvious seasonality. Thus, their effect on the HCHO seasonality can be probably ignored. Fourth, biogenic primary emissions of HCHO could be another factor contributing to the HCHO seasonality due to its significant differences between in summer and winter (Chen et al., 2014).

3) Aerosols

The local aerosol sources, including primary aerosol emissions and secondary aerosol formations, and transport of aerosols can in principle both contribute to the local aerosol amount. The contribution of transported aerosols has an obvious seasonality: In May and June, the transport from biomass burning might contribute to up to 37% of the $PM_{2.5}$ amount based on a case study in summer 2011 (Cheng et al., 2014). In spring and autumn dust storms from Mongolia can reach Wuxi (Liu et al., 2012; Fu et al., 2014b and Li et al., 2014). The polluted air from the eastern area (for example, Shanghai) and northern area (for example Jing–Jin–Ji region) (Jiang et al., 2015) could also move to Wuxi under appropriate meteorological conditions (Liu et al., 2012). Haze events frequently occur in autumn and winter (Fu et al., 2014a).

The inter-annual trends of TGs and aerosols are presented in Fig. 12. Because of missing observations in some months and inner-annual variations of abundances of the species, only data from May to November are used. SO_2 shows a clear decreasing trend from 2011 to 2014. However NO_2, HCHO and aerosols almost maintain constant amounts.

The monthly mean profiles of NO_2, SO_2 and HCHO (under clear and cloudy sky conditions except thick clouds and fog) and aerosols (only under clear sky conditions) (screened by the scheme in Table 3) are presented in Fig. 13. The monthly mean TG profiles under clear sky conditions (see Fig. S27 in the supplement) are almost identical to those under various sky

conditions except fog and thick clouds. During all seasons, NO_2 shows an exponentially decreasing profile (see Fig. 13a). On average the NO_2 VMR at 0.5 km is about half of the near-surface VMR and it rapidly decreases above 0.5km to about 2 ppb at 1.5 km. Aircraft measurements of NO_x in October 2007 in the Yangtze River Delta region by Geng et al. (2009) presented similar vertical profiles. The profile shape of NO_2 can be mostly attributed to its near-surface emission sources and short life
5 time.

The SO_2 layer is found at a higher altitude compared to NO_2 (see Fig. 13b). A more box-like shape up to the altitude of about 0.7km to 1km is found in autumn and winter when the SO_2 load is large and also long-range transport might effectively contribute to the SO_2 amounts in Wuxi. In contrast, for the rather small SO_2 loads in summer, an exponential profile shape is found. Similar profile shapes are also obtained from aircraft measurements during September to October of 2007 over Wuxi
10 (Xue et al., 2009). One interesting finding is the lofted SO_2 layer at around 0.7 km in February and March 2012, which is probably related to long distance transport from a heavily polluted region. This interpretation is supported by the dominating wind direction (coming from the nearby polluted area around Shanghai) in March 2012 (see Fig. S28 of the supplement) compared to other years.

In all seasons, the HCHO profile shape consists of three parts (see Fig. 13c): a decrease from the surface to about 0.3 km, an
15 almost constant value from about 0.3 km to about 1.1 km, and a steep decrease above. The high values at the surface are probably caused by primary emissions and rapid formation from particular VOCs near the surface. Transport of longer lived VOCs to higher altitudes and subsequent destruction probably contributes to the increased values at up to about 1 km. While other measurements of tropospheric profiles of HCHO are not available around Wuxi, it is still reasonable to compare our results with the aircraft measurements of HCHO over Bresso near Milano during summer of 2003 (Junkermann, 2009;
20 Wagner et al., 2011) because both of the measurements took place in polluted urban regions. They found a layer height with high HCHO concentration values of up to 1km and the highest values were found normally close to the ground. This feature is consistent with our results in Wuxi. However it should be noted that VMRs of HCHO at high altitudes are strongly constrained by the a-priori profiles because of the low sensitivity of MAX-DOAS retrievals at these altitudes. More comparison studies with aircraft measurements need to be done in the future to further quantify the retrieval sensitivities for
25 elevated layers. Nevertheless we still have confidence in the extended vertical distribution of HCHO retrieved by MAX-DOAS for two reasons: 1) the Fig. S9 in the supplement indicates the higher vertical extension can be partly represented even for using an exponential a-priori profile; 2) a large variability of HCHO VMRs at the altitude around 1km is retrieved from MAX-DOAS observations. This indicates that the sensitivity of MAX-DOAS retrievals to the elevated layers is still large enough.

30 Figure 13d shows the aerosol profiles representing a box-like shape near the surface and an exponential decrease above 0.5 to 1 km. The box-like part in winter is systematically lower than in other seasons probably due to the lower BL in winter. Baars et al. (2008) reported such a seasonal dependence of the top height of the BL obtained from lidar observations in Germany over a one-year period. A similar seasonal dependence of the BL can be expected in Wuxi. From May to October

the highest AE is found at an elevated altitude of up to 0.7km, especially in 2014. This feature could indicate long distance transports of aerosols, probably from biomass burning events.

3.2 Diurnal variations of NO_2, SO_2, HCHO and aerosols

Figure 14 shows the seasonally averaged diurnal variations of TG VCDs and near-surface VMRs as well as AODs and near-surface AE from 2011 to 2014. The morning and afternoon averaged profiles of aerosols and TGs are also shown in winter and summer, respectively, in Fig. S29 in the supplement. The diurnal variations can probably be attributed to the complex interaction of the primary and secondary sources, deposition and atmospheric transport processes in the BL. The diurnal variation of the BL height (Baars et al., 2008) can systematically affect the diurnal patterns of near-surface VMRs and AE, but has almost no impact on the TG VCDs and AOD.

As seen in Fig. 14a, the seasonality of the diurnal variation of the NO_2 VCDs is quite similar to the MAX-DOAS observations in Beijing (Ma et al., 2013). They conclude that the phenomenon is probably caused by the complex interplay of the emission, chemistry and transport, with generally higher emission rates and a longer NO_2 lifetime in winter. In Fig. 14b, the SO_2 VCD shows almost constant values during the whole day in summer (with a slight decrease in the afternoon). In winter high values persist until 13:00 LT and then rapidly decrease. In autumn and spring the highest values occur around noon. The SO_2 variation mostly happens in the layer below 0.5 km (see Fig. S29 in the supplement). The variation features are different from the observations in Beijing (Wang et al., 2014a), probably caused by different sources, transport and life time at the two locations. In Fig. 14c it is shown that the HCHO VCDs increase rapidly after sunrise with a faster increase in summer. HCHO has a stronger variation at the layer from 0.5km to 1km. This diurnal pattern is probably mainly related to the photochemical formation of HCHO and the VOCs emitted by vehicles and biogenic emissions (Kesselmeier and Staudt, 1999). In Fig. 14d similar relative diurnal variations of AODs and AE are found for the different seasons. Their diurnal variations can be affected by various factors, e.g. the diurnal variation of the emission sources, as well as secondary formation, deposition and dispersion.

3.3 Weekly cycles of NO_2, SO_2, HCHO and aerosol extinction

In urban areas, anthropogenic sources often control the amounts of pollutants. Because human activities are usually strongest during the working days, weekly cycles of NO_2, SO_2, HCHO and aerosols can provide information on the contributions from natural and anthropogenic sources (Beirle et al., 2003 and Ma et al., 2013). Weekly cycles are found for NO_2 and SO_2 as shown in Fig. 15. The relative differences of the VCDs and near-surface VMRs between the average working day level (from Monday to Friday) and the value on Sunday are 11% and 18% for NO_2, 13% and 11% for SO_2, respectively. For HCHO smaller weekly cycles (7% of VCD and 12% of near-surface VMR) are found. In contrast, no clear weekend reduction is found for aerosols. The negligible weekly cycle of aerosols is probably caused by the rather long life time of aerosols and the effect of long-range transport, e.g. from biomass burning and dust. Figure S30 of the supplement shows that

the diurnal variations of the three TGs are almost the same on different days of the week indicating similar sources during the working days and weekends.

3.4 Source analysis of the pollutants

3.4.1 Relation between the precursors and aerosols

5   Huang et al. (2014) showed that secondary aerosols including organic and inorganic aerosols (nitrates and sulfates) contribute to about 74% of the $PM_{2.5}$ mass collected during high pollution events in January 2013 at the urban site of Shanghai. The aerosols in Wuxi (which is close to Shanghai) are expected to be similarly dominated by secondary aerosol. NO_x and SO_2 are the precursors of secondary inorganic aerosols through their conversion into nitrates and sulfates, respectively. HCHO can be used as a proxy for the local amount of VOCs, which are precursors of secondary organic

10   aerosols (Claeys et al., 2004). To identify the dominant precursor, we investigated the relationship between aerosols and their precursors through a correlation study as in Lu et al. (2010), Veefkind et al. (2011) and Wang et al. (2014a). Table 5 lists the correlation coefficients between the TG VCDs and AODs as well as the TG VMRs and AE near the surface. The correlations of near-surface values are always higher than those of the column densities. This finding could be probably explained by the effect of long-range transport, which typically occurs at elevated layers. For long-range transport, the effect

15   of different atmospheric lifetimes is especially large probably leading to weaker correlations between the aerosol and its precursors. In contrast, close to the surface, local emissions dominate the concentrations of TG and aerosols and the effect of different lifetimes is negligible.

  In general, correlations in spring are the lowest probably due to the transport of dust and biomass burning aerosols. The correlations between aerosols and HCHO are higher in winter than in summer. This finding may be explained by the fact that

20   anthropogenic emissions dominate the (primary and secondary) sources of HCHO and aerosols simultaneously in winter. Meanwhile the correlations between aerosols and HCHO are higher than those between aerosols and NO_2 or SO_2 in winter and autumn. This finding can be possibly explained by the fact that both HCHO and aerosols are dominated by secondary sources, while NO_2 and SO_2 are mostly from primary emissions in this region.

3.4.2 Wind dependence of the pollutants

25   The MAX-DOAS station is located on the boundary of urban and suburban areas as shown in Fig. 1b. Several iron factories, cement factories, and petroleum industries are operated in the south-west industrial area. The industrial activities and vehicle operations in the industrial area lead to significant emissions of NO_2, SO_2, VOCs as well as aerosols (Huang et al., 2011). In the urban centre area, traffic, construction sites and other anthropogenic emissions emit significant amounts of NO_2, VOCs as well as particles. Some factories, such as an oil refinery, are located in the north-west of the urban centre, emitting

30   pollutants including SO_2 and VOCs. In addition, one power plant located at about 50km in the north and the Suzhou city in

the south-east direction of the MAX-DOAS station might contribute to the observed pollutants in Wuxi depending on the meteorological condition.

We analysed the distributions of column densities and near-surface values of the TGs and aerosols for different wind directions in Fig. 16. In principle, the near surface pollutants are expected to be dominated by nearby emission sources, while the column densities can be additionally affected by transport of pollutants from remote sources. Long-range transport can weaken the dependence of the column densities on the wind direction because of the complex trajectories the air masses might have followed. For all four species, the highest values are observed for south-westerly winds, especially for the near-surface pollutants. This finding implies that the industrial area emits large amounts of NO_x, SO_2, VOCs and aerosols. Fig. 16c shows that the HCHO southwest peak is only present in winter. This finding is probably caused by the fact that in winter anthropogenic sources (of precursors and direct HCHO emissions) dominate the HCHO amounts, while in other seasons natural sources dominate the HCHO amounts. Another peak of NO_2 and SO_2 is found in the northwest, obviously in winter, indicating considerable emissions in the urban centre. Fig 16d shows a weaker dependence of AODs on the wind direction than the VCDs of the TGs, which probably indicates the stronger contribution of long-range transport to the local aerosol levels compared to the TGs. In addition for daily averaged wind speed of smaller than 1 m/s, the averaged TGs VCDs and near-surface VMRs are higher than those for larger wind speeds (shown in Fig. S31a and b), indicating that dispersion of local emissions is more important than the transport from distant sources. For aerosols, a wind speed dependency is only observed for near-surface AE, but not for AODs (see Fig. S31c), indicating the higher importance of transport for aerosols than for TGs.

Although local, this study shows several general important features: 1) the dependence of the measured TG VMRs on the wind direction indicates that the dominating sources of the pollution are local, and not from long range transport. Also, a strong horizontal gradient appears. Because of the expected similar life time, meteorological conditions and emission sources, the conclusion could apply to the whole YRD region. 2) The study provides an example on how to use ground-based MAX-DOAS observations to find strong emission sources in an urban-size area. 3) The seasonality of the wind dependence of the trace gases, especially for HCHO, indicates the different sources in different seasons.

4 Conclusions

The long-term characteristics of the spatial and temporal variation of NO_2, SO_2, HCHO and aerosols in Wuxi (part of the Yangtze River delta region) are characterized by automatic MAX-DOAS observations from May 2011 to Dec 2014. The PriAM OE-based algorithm was applied to the MAX-DOAS observations to acquire vertical profiles, VCDs (AODs) and near-surface VMRs (AE) of TGs (aerosols) in the layer from the surface to an altitude of about 4 km.

The AODs and near-surface AE and the VMRs of NO_2 and SO_2 from MAX-DOAS are compared with coincident data sets (for one year) obtained by a sun photometer at the AERONET Taihu station, a nearby visibility meter and a LP-DOAS, respectively. In general good agreement was found: under clear sky conditions, correlation coefficients of 0.56−0.91 for

AODs, 0.31−0.71 for AE, 0.42−0.64 for NO_2 VMRs and 0.68−0.81 for SO_2 VMRs as well as the low systematic bias of -0.16−0.029 (<20%) for AODs, 0.05−0.19 km^{-1} (<33%) for AE, -2.23−5.11 ppb (<50%) for NO_2 VMRs and 1.8−6.1 ppb (<60%) for SO_2 VMRs are found in different seasons.

Further comparisons were performed for different cloud conditions identified by the MAX-DOAS cloud classification scheme. For most cloud conditions (except optically thick clouds and fog) similar agreement as for clear sky conditions is found for the results of near-surface TG VMRs and AE. However, the AOD results are more strongly affected by clouds and we recommend to only retrieving near-surface AE for cloudy observations. In the presence of fog and optically thick clouds, no meaningful profile inversions for TGs and aerosols are possible. Thus for further interpretations, we considered TG results and near-surface AE for clear and cloudy sky conditions (except fog and optically thick clouds), but AOD only for clear sky conditions.

In this study we also investigated two important aspects of the MAX-DOAS data analysis: For the first time the effect of the seasonality of temperature and pressure on the MAX-DOAS retrievals of aerosols was investigated. Such an effect is especially important for the measurements in Wuxi, because strong and systematic variations of temperature and pressure are regularly found. Accordingly the O_4 VCD changes systematically with seasons, which was in our study for the first time explicitly taken into account for the aerosol profile retrieval. It was shown that without this correction, deviations of the AOD of up to 20% can occur.

Moreover, we systematically compared trace gas VCDs derived either by the so-called geometric approximation with those derived by integration of the derived vertical profiles. Such discrepancies were reported in previous studies. We could show that the difference between both methods can be clearly assigned to limitations of the geometric approximation. This error becomes especially significant when the aerosol load is strong, which is the situation in most industrialised regions. Thus we conclude that in general the integration of the retrieved profiles is the more exact way to extract the tropospheric TG VCDs, and we used this method in this study.

A prominent seasonality of all TGs is found in agreement with many previous studies based on satellite and ground-based observations. NO_2 and SO_2 have maxima and minima in winter and summer, respectively, while HCHO has an opposite seasonality. No pronounced seasonality of aerosols is found. From 2011 to 2014, only SO_2 shows a clear decreasing trend, while NO_2, HCHO and aerosol levels stay almost constant.

Different profile shapes are found for the different species: for NO_2 exponentially decreasing profiles with a scale height of about 0.6km are observed in different seasons. SO_2 profiles extend to slightly higher altitudes than NO_2, probably due to the longer lifetime of SO_2. Especially in winter often elevated layers of enhanced SO_2 are found between about 0.7km and 1km (especially in early 2012), probably indicating the importance of long range transport of SO_2. HCHO reaches up to even higher altitudes (up to > 1 km) than NO_2 and SO_2, probably indicating the effect of the secondary formation from VOCs. However, typically the largest HCHO VMRs are still found near the surface (like for NO_2 and SO_2). The aerosol profiles typically show constant values close to the surface (below about 0.5km), but decrease exponentially above that layer. Especially in winter often elevated layers (between 0.5km and 0.7km) are observed.

Different diurnal variations are found for the different species: For the NO_2 VCDs, depending on season, a decrease or increase is found during the day. For the NO_2 VMRs and SO_2 VCDs and VMRs, typically a slight decrease during the day is observed. The diurnal variations of HCHO and aerosols are more complex and show a pronounced maximum around noon in summer indicating photochemical production. Systematic weekly cycles occur for NO_2 and SO_2 with the maximum values on Thursday or Friday and minimum values on Sunday indicating a large contribution of anthropogenic emissions. In contrast, the amplitudes of the weekly cycles for HCHO and aerosols are rather small.

We performed correlation analyses between the different TG results versus the aerosol results for individual seasons. For all TGs and seasons positive correlations (correlation coefficient between 0.12 and 0.65) were found with the highest correlations in winter. In general the highest correlation is found for HCHO in winter probably indicating a similar secondary formation process for both species. In general, higher correlations are found for the near-surface products (VMRs versus AE) compared to the column products (VCDs versus AOD).

We found a clear wind direction dependence of TG and aerosols results, especially for the near-surface concentrations. The dependencies indicate that the largest sources of the observed pollutants in Wuxi are anthropogenic emissions from the nearby industrial area (including traffic emissions). In addition the obvious lower TG results for high wind speed than for low wind speed indicate that the dispersion of local emissions is more important than the transport from distant sources. Interestingly, for HCHO, a considerable dependence on the wind direction is only observed in winter probably indicating significant VOC emissions from natural sources in the growing seasons.

The data sets of the TGs and aerosols are also valuable to validate tropospheric products from satellite observations and chemical transport models. This study is in progress.

Acknowledgements: We thank the Wuxi CAS Photonics Co. Ltd for their contributions to operate the observations of the MAX-DOAS instrument, the long path DOAS instrument, the visibility meter and the weather station in Wuxi. We thank the Institute of Remote Sensing / Institute of Environmental Physics, University of Bremen, Bremen, Germany for their freely accessible radiative transfer model SCIATRAN. We thank Belgian Institute for Space Aeronomy (BIRA-IASB), Brussels, Belgium for their freely accessible WINDOAS software and generating the mean map of SO_2 and HCHO tropospheric VCDs derived from OMI observations over eastern China. We thank Goddard Space Flight Center, NASA for their freely accessible archive of AERONET data. We thank Prof. Ma Ronghua in Nanjing Institute of Geography & Limnology Chinese Academy of Sciences for his effort to operate the Taihu AERONET station. We thank Royal Netherlands Meteorological Institute for their freely accessible archive of OMI tropospheric NO_2 data. We thank Trissevgeni Stavrakou in BIRA-IASB, Hang Su and Yafang Cheng in MPIC for their help to interpret the correlations between aerosols and the trace gases. This work was supported by Max Planck Society-Chinese Academy of Sciences Joint Doctoral Promotion Programme, and National Natural Science Foundation of China (Grant No.: 41275038 and 41530644) and Monitoring and Assessment of Regional air quality in China using space Observations, Project Of Long-term sino-european co-Operation (MarcoPolo), FP7 (Grant No: 606953).

References

Aliwell, S. R., Van Roozendael, M., Johnston, P. V., Richter, A., Wagner, T., Arlander, D. W., Burrows, J. P., Fish, D. J., Jones, R. L., Tørnkvist, K. K., Lambert, J.-C., Pfeilsticker, K., and Pundt, I.: Analysis for BrO in zenith-sky spectra: An intercomparison exercise for analysis improvement, J. Geophys. Res., 107, D140, doi:10.1029/2001JD000329, 2002.

Ahmed, A.A., Mohamed, A., Ali, A.E., Barakat, A., El-Hady, M.A. and El-Hussein, A.: Seasonal variations of aerosol residence time in the lower atmospheric boundary layer, Journal of environmental radioactivity, 77(3), 275-283, 2004.

Baars, H., Ansmann, A., Engelmann, R., and Althausen, D.: Continuous monitoring of the boundary-layer top with lidar, Atmos. Chem. Phys., 8, 7281-7296, doi:10.5194/acp-8-7281-2008, 2008.

Beirle, S., Platt, U., Wenig, M., and Wagner, T.: Weekly cycle of NO_2 by GOME measurements: a signature of anthropogenic sources, Atmos. Chem. Phys., 3, 2225–2232, doi: 10.5194/acp-3-2225-2003, 2003.

Beirle, S., Boersma, K. F., Platt, U., Lawrence, M. G., and Wagner, T.: Megacity emissions and lifetimes of nitrogen oxides probed from space, Science, 333, 1737–1739, 2011.

Beirle, S., Hörmann, C., Penning de Vries, M., Dörner, S., Kern, C., and Wagner, T.: Estimating the volcanic emission rate and atmospheric lifetime of SO2 from space: a case study for Kīlauea volcano, Hawai`i, Atmos. Chem. Phys., 14, 8309-8322, doi:10.5194/acp-14-8309-2014, 2014.

Bobrowski, N., Honninger, G., Galle, B. and Platt, U.: Detection of bromine monoxide in a volcanic plume, Nature, 423, 273–276, 2003.

Boersma, K. F., Eskes, H. J., Veefkind, J. P., Brinksma, E. J., van der A, R. J., Sneep, M., van den Oord, G. H. J., Levelt, P. F., Stammes, P., Gleason, J. F. and Bucsela, E. J.: Near-real time retrieval of tropospheric NO2 from OMI, Atmos. Chem. Phys., 7, 2103–2118, 2007.

Boersma, K.F., H.J. Eskes, R. J. Dirksen, R. J. van der A, J. P. Veefkind, P. Stammes, V. Huijnen, Q. L. Kleipool, M. Sneep, J. Claas, J. Leitao, A. Richter, Y. Zhou, and D. Brunner, An improved retrieval of tropospheric NO2 columns from the Ozone Monitoring Instrument, Atmos. Meas. Tech. , 4, 1905-1928, 2011.

Bogumil, K., Orphal, J., Homann, T., Voigt, S., Spietz, P., Fleischmann, O. C., Vogel, A., Hart-mann, M., Kromminga, H., Bovensmann, H., Frerick, J., and Burrows, J. P.: Measurements of molecular absorption spectra with the SCIAMACHY pre-flight model: instrument characterization and reference data for atmospheric remote-sensing in the 230–2380 nm region, J. Photoch. Photobio. A, 157, 167–184, 2003.

Brinksma, E. J., Pinardi, G., Volten, H., Braak, R., Richter, A., Schönhardt, A., van Roozendael, M., Fayt, C., Hermans, C., Dirksen, R. J., Vlemmix, T., Berkhout, A. J. C., Swart, D. P. J., Oetjen, H., Wittrock, F., Wagner, T., Ibrahim, O. W., de Leeuw, G., Moerman, M., Curier, R. L., Celarier, E. A., Cede, A., Knap, W. H., Veefkind, J. P., Eskes, H. J., Allaart, M., Rothe, R., Piters, A. J. M., and Levelt, P. F.: The 2005 and 2006 DANDELIONS NO_2 and aerosol intercomparison campaigns, J. Geophys. Res., 113, D16S46, 2008.

Chen, W. T., Shao, M., Lu, S. H., Wang, M., Zeng, L. M., Yuan, B., and Liu, Y.: Understanding primary and secondary sources of ambient carbonyl compounds in Beijing using the PMF model, Atmos. Chem. Phys., 14, 3047-3062, doi:10.5194/acp-14-3047-2014, 2014.

Cheng, Z., Wang, S., Fu, X., Watson, J. G., Jiang, J., Fu, Q., Chen, C., Xu, B., Yu, J., Chow, J. C., and Hao, J.: Impact of biomass burning on haze pollution in the Yangtze River delta, China: a case study in summer 2011, Atmos. Chem. Phys., 14, 4573-4585, doi:10.5194/acp-14-4573-2014, 2014.

Claeys, M., Graham, B., Vas, G., Wang, W., Vermeylen, R., Pashyn-ska, V., Cafmeyer, J., Guyon, P., Andreae, M. O., Artaxo, P., and Maenhaut, W.: Formation of secondary organic aerosols through photooxidation of isoprene, Science, 303, 1173–1176, 2004.

Clémer, K., Van Roozendael, M., Fayt, C., Hendrick, F., Hermans, C., Pinardi, G., Sperr, R., Wang, P., and De Maziere, M.: Multiple wavelength retrieval of tropospheric aerosol optical properties from MAXDOAS measurements in Beijing, Atmos. Meas. Tech., 3, 863–878, 2010.

Crippa, M., Ciarelli, G., Piazzalunga, A., Schwikowski, M., Abbaszade, G., Schnelle-Kreis, J., Zimmermann, R., An, Z., Szidat, S., Baltensperger, U., El Haddad, I., and Prevot, A. S.: High secondary aerosol contribution to particulate pollution during haze events in China, Nature, 514, 218–222, 2014.

De Smedt, I., Stavrakou, T., Müller, J. F., van der A, R. J., and Van Roozendael, M.: Trend detection in satellite observations of formaldehyde tropospheric columns, Geophys. Res. Lett., 37(18), L18808, doi:10.1029/2010GL044245, 2010.

De Smedt, I., Stavrakou, T., Hendrick, F., Danckaert, T., Vlemmix, T., Pinardi, G., Theys, N., Lerot, C., Gielen, C., Vigouroux, C., Hermans, C., Fayt, C., Veefkind, P., Müller, J.-F., and Van Roozendael, M.: Diurnal, seasonal and long-term variations of global formaldehyde columns inferred from combined OMI and GOME-2 observations, Atmos. Chem. Phys., 15, 12519-12545, doi:10.5194/acp-15-12519-2015, 2015.

Environmental Protection Agency: National air quality and emissions trends report 1998, Rep. EPA 454/R-00-003, 1998.

Erle F., Pfeilsticker K., Platt U, On the influence of tropospheric clouds on zenith scattered light measurements of stratospheric species, Geophys. Res. Lett., 22, 2725-2728, 1995.

Fayt, C. and van Roozendael, M.: WinDOAS 2.1 Software User Manual, IASB/BIRA (http://www.oma.be/GOME/GOMEBrO/WinDOAS-SUM-210b.pdf), 2009.

Frieß, U., Monks, P. S., Remedios, J. J., Rozanov A., Sinreich R., Wagner T., and Platt, U.: MAX-DOAS O_4 measurements: A new technique to derive information on atmospheric aerosols: 2. Modeling studies, J. Geophys. Res., 111, D14203, 2006, doi:10.1029/2005JD006618.

Frieß U, Sihler H, Sander R. The vertical distribution of BrO and aerosols in the Arctic: Measurements by active and passive differential optical absorption spectroscopy, J. Geophys. Res., 116, D00R04, 2011.

Frieß, U., Klein Baltink, H., Beirle, S., Clémer, K., Hendrick, F., Henzing, B., Irie, H., de Leeuw, G., Li, A., Moerman, M. M., van Roozendael, M., Shaiganfar, R., Wagner, T., Wang, Y., Xie, P., Yilmaz, S., and Zieger, P.: Intercomparison of

aerosol extinction profiles retrieved from MAX-DOAS measurements, Atmos. Meas. Tech. Discuss., doi:10.5194/amt-2015-358, 2016.

Fu, X., Wang, S., Zhao, B., Xing, J., Cheng, Z., Liu, H., and Hao, J.: Emission inventory of primary pollutants and chemical speciation in 2010 for the Yangtze River Delta region, China, Atmos. Environ., 70, 39–50, doi:10.1016/j.atmosenv.2012.12.034, 2013.

Fu, G. Q., Xu, W. Y., Yang, R. F., Li, J. B., and Zhao, C. S.: The distribution and trends of fog and haze in the North China Plain over the past 30 years, Atmos. Chem. Phys., 14, 11949-11958, doi:10.5194/acp-14-11949-2014, 2014a.

Fu, X., Wang, S. X., Cheng, Z., Xing, J., Zhao, B., Wang, J. D., and Hao, J. M.: Source, transport and impacts of a heavy dust event in the Yangtze River Delta, China, in 2011, Atmos. Chem. Phys., 14, 1239-1254, doi:10.5194/acp-14-1239-2014, 2014b.

Geng, F., Zhang, Q., Tie, X., Huang, M., Ma, X., Deng, Z., Yu, Q., Quan, J., Zhao, C.: Aircraft measurements of O3, NOx, CO, VOCs, and SO2 in the Yangtze River Delta region. Atmospheric Environment, 43(3), 584-593, 2009.

Hartl, A. and Wenig, M. O.: Regularisation model study for the least-squares retrieval of aerosol extinction time series from UV/VIS MAX-DOAS observations for a ground layer profile parameterisation, Atmos. Meas. Tech., 6, 1959-1980, doi:10.5194/amt-6-1959-2013, 2013.

Hendrick, F., Müller, J.-F., Clémer, K., Wang, P., De Mazière, M., Fayt, C., Gielen, C., Hermans, C., Ma, J. Z., Pinardi, G., Stavrakou, T., Vlemmix, T., and Van Roozendael, M.: Four years of ground-based MAX-DOAS observations of HONO and NO2 in the Beijing area, Atmos. Chem. Phys., 14, 765-781, doi:10.5194/acp-14-765-2014, 2014.

Hendrick, F., Gielen, C., Lerot, C., Stavrakou, T., De Smedt, I., Fayt, C., Hermans, C., Müller, J. F., Pinardi, G., Volkamer, R., Wang, P., and Van Roozendael, M.: Retrieval of CHOCHO from MAX-DOAS measurements in the Beijing area, 7th DOAS workshop 2015, Brussels, Belgium, 7 July 2015.

Henyey, L. G. and Greenstein J. L.: Diffuse radiation in the galaxy, Astrophysical Journal, 93, 70-83, 1941.

Ho, K. F., Lee, S. C., Louie, P. K. K., and Zou, S. C.: Seasonal variation of carbonyl compound concentrations in urban area of Hong Kong, Atmos. Environ., 36, 1259–1265, 2002.

Holben, B. N., Eck, T. F., Slutsker, I., Tanre, D., Buis, J. P., Set-zer, A., Vermote, E., Reagan, J. A., Kaufman, Y., Nakajima, T., Lavenu, F., Jankowiak, I., and Smirnov, A.: AERONET – A federated instrument network and data archive for aerosol characterization, Remote Sens. Environ., 66, 1–16, 1998.

Holben, B. N., Tanre, D., Smirnov, A., Eck, T. F., Slutsker, I., Abuhassan, N., Newcomb, W. W., Schafer, J., Chatenet, B., Lav-enue, F., Kaufman, Y. J., Van de Castle, J., Setzer, A., Markham, B., Clark, D., Frouin, R., Halthore, R., Karnieli, A., O'Neill, N. T., Pietras, C., Pinker, R. T., Voss, K., and Zibordi, Z.: An emerging ground-based aerosol climatology: Aerosol optical depth from AERONET, J. Geophys. Res., 106, 12067–12097, 2001

Hönninger, G. and Platt, U.: Observations of BrO and its vertical distribution during surface ozone depletion at Alert, Atmos. Environ., 36, 2481–2489, 2002.

Hönninger, G., Friedeburg, C. von and Plat, U., Multi axis differential optical absorption spectroscopy (MAX-DOAS), Atmos. Chem. Phys., 4, 231–254, 2004

Huang, C., Chen, C. H., Li, L., Cheng, Z., Wang, H. L., Huang, H. Y., Streets, D. G., Wang, Y. J., Zhang, G. F., and Chen, Y. R.: Emission inventory of anthropogenic air pollutants and VOC species in the Yangtze River Delta region, China, Atmos. Chem. Phys., 11, 4105-4120, doi:10.5194/acp-11-4105-2011, 2011.

Huang, R.-J., Zhang, Y., Bozzetti, C., Ho, K.-F., Cao, J., Han, Y., Dällenbach, K. R., Slowik, J. G., Platt, S. M., Canonaco, F., Zotter, P., Wolf, R., Pieber, S. M., Bruns, E. A., Crippa, M., Ciarelli, G., Piazzalunga, A., Schwikowski, M., Abbaszade, G., Schnelle-Kreis, J., Zimmermann, R., An, Z., Szidat, S., Baltensperger, U., Haddad, I. E., and Prévôt, A. S. H.: High secondary aerosol contribution to particulate pollution during haze events in China, Nature, 514, 218–222, 2014.

Irie, H., Kanaya, Y., Akimoto, H., Iwabuchi, H., Shimizu, A., and Aoki, K.: First retrieval of tropospheric aerosol profiles using MAX-DOAS and comparison with lidar and sky radiometer measurements, Atmos. Chem. Phys., 8, 341–350, 2008.

Irie, H., Takashima, H., Kanaya, Y., Boersma, K. F., Gast, L., Wittrock, F., Brunner, D., Zhou, Y., and Van Roozendael, M.: Eight-component retrievals from ground-based MAX-DOAS observations, Atmos. Meas. Tech., 4, 1027–1044, 2011.

Jiang, C., Wang, H., Zhao, T., Li, T., and Che, H.: Modeling study of PM2.5 pollutant transport across cities in China's Jing–Jin–Ji region during a severe haze episode in December 2013, Atmos. Chem. Phys., 15, 5803-5814, doi:10.5194/acp-15-5803-2015, 2015.

Junkermann, W.: On the distribution of formaldehyde in the western Po-Valley, Italy, during FORMAT 2002/2003, Atmos. Chem. Phys., 9, 9187–9196, doi:10.5194/acp-9-9187-2009, 2009.

Kanaya, Y., Irie, H., Takashima, H., Iwabuchi, H., Akimoto, H., Sudo, K., Gu, M., Chong, J., Kim, Y. J., Lee, H., Li, A., Si, F., Xu, J., Xie, P.-H., Liu, W.-Q., Dzhola, A., Postylyakov, O., Ivanov, V., Grechko, E., Terpugova, S., and Panchenko, M.: Long-term MAX-DOAS network observations of NO2 in Russia and Asia (MADRAS) during the period 2007–2012: instrumentation, elucidation of climatology, and comparisons with OMI satellite observations and global model simulations, Atmos. Chem. Phys., 14, 7909-7927, doi:10.5194/acp-14-7909-2014, 2014.

Kesselmeier, J. and Staudt, M.: Biogenic volatile organic compounds (VOC): an overview on emission, physiology and ecology. J. Atmos. Chemistry 33, 23-88, 1999.

Kraus, S.: DOASIS, A Framework Design for DOAS, PhD-thesis, University of lMannheim,http://hci.iwr.uni-heidelberg.de/publications/dip/2006/Kraus_PhD2006.pdf, 2006.

Lee, C., Martin, R. V., van Donkelaar, A., Lee, H., Dicker-son, R. R., Hains, J. C., Krotkov, N., Richter, A., Vinnikov, K., and Schwab, J. J.: SO$_2$ emissions and lifetimes: Estimates from inverse modeling using in situ and global, space–based (SCIAMACHY and OMI) observations, J. Geophys. Res., 116, D06304, doi:10.1029/2010JD014758, 2011.

Levelt, P. F., Hilsenrath, E., Lepppelmeier, G. W., van den Oord, G. H. J., Bhartia, P. K., Taminnen, J., de Haan, J. F. and Veefkind, J. P.: Science objectives of the Ozone Monitoring Instrument, IEEE Trans. Geosci. Remote Sens., 44, 1199, 2006a.

Levelt, P. F., van den Oord, G. H. J., Dobber, M. R., Malkki, A., Visser, H., de Vries, J., Stammes, P., Lundell, J. and Saari, H.: The Ozone Monitoring Instrument, IEEE Trans. Geosci. Remote Sens., 44, 1093, 2006b.

Li X., Brauers, T. and Hofzumahaus, A.: MAX-DOAS measurements of NO2, HCHO and CHOCHO at a rural site in Southern China. Atmos. Chem. Phys. Discuss., 12, 3983-4029, 2012.

Li X., Brauers, T., Shao, M., Garland, R. M., Wagner, T., Deutschmann, T., and Wahner, A.: MAX-DOAS measurements in southern China: retrieval of aerosol extinctions and validation using ground-based in-situ data. Atmos. Chem. Phys., 10, 2079–2089, 2010.

Li, G. L., Zhou, M., Chen, C. H., Wang, H. L., Wang, Q., Lou, S. R., .Qiao, L. P., Tang, X. B., Li, L., Huang H. Y., Chen M., H., Huang C., and Zhang, G. F.: Characteristics of particulate matters and its chemical compositions during the dust episodes in Shanghai in spring, 2011, Environmental Science, 35(5), 1644-1653, 2014

Lin, W., Xu, X., Ge, B., and Liu, X.: Gaseous pollutants in Beijing urban area during the heating period 2007–2008: variability, sources, meteorological, and chemical impacts, Atmos. Chem. Phys., 11, 8157–8170, doi:10.5194/acp-11-8157-2011, 2011.

Liu, F., Beirle, S., Zhang, Q., Dörner, S., He, K. B., and Wagner, T.: NOx lifetimes and emissions of hotspots in polluted background estimated by satellite observations, Atmos. Chem. Phys. Discuss., 15, 24179-24215, doi:10.5194/acpd-15-24179-2015, 2015.

Liu, J., Zheng, Y., Li, Z., Flynn, C., and Cribb, M.: Seasonal variations of aerosol optical properties, vertical distribution and associated radiative effects in the Yangtze Delta region of China. Journal of Geophysical Research: Atmospheres (1984–2012), 117(D16), 2012.

Lu, Z., Streets, D. G., Zhang, Q., Wang, S., Carmichael, G. R., Cheng, Y. F., Wei, C., Chin, M., Diehl, T., and Tan, Q.: Sulfur dioxide emissions in China and sulfur trends in East Asia since 2000, Atmos. Chem. Phys., 10, 6311–6331, doi:10.5194/acp-10-6311-2010, 2010.

Ma, J. Z., Beirle, S., Jin, J. L., Shaiganfar, R., Yan, P., and Wagner, T.: Tropospheric NO2 vertical column densities over Beijing: results of the first three years of ground-based MAX-DOAS measurements (2008–2011) and satellite validation, Atmos. Chem. Phys., 13, 1547-1567, doi:10.5194/acp-13-1547-2013, 2013.

Meller, R. and Moortgat, G. K.: Temperature dependence of the ab-sorption cross sections of formaldehyde between 223 and 323 K in the wavelength range 225–375 nm, J. Geophys. Res., 105, 7089–7101, 2000

Meng, Z. Y., Ding, G. A., Xu, X. B., Xu, X. D., Yu, H. Q., and Wang, S. F.: Vertical distributions of SO2 and NO2 in the lower atmosphere in Beijing urban areas, China. Science of the Total Environment, 390(2), 456-465, 2008.

Nasse, J. M., Zielcke, J., Frieß, U., Lampel, J., König-Langlo, G. and Platt, U.: Inference of cloud altitude and optical properties from MAX-DOAS measurements, EGU General Assembly 2015, Wien, 12 April 2015 - 17 April 2015, hdl:10013/epic.45412, http://hdl.handle.net/10013/epic.45412.

Oppenheimer, C., Francis, P., and Stix, J.: Depletion rates of sulfur dioxide in tropospheric volcanic plumes, Geophys. Res. Lett., 25, 2671–2674, doi:10.1029/98GL01988, 1998.

Pinardi, G., Van Roozendael, M., Abuhassan, N., Adams, C., Cede, A., Clémer, K., Fayt, C., Frieß, U., Gil, M., Herman, J., Hermans, C., Hendrick, F., Irie, H., Merlaud, A., Navarro Comas, M., Peters, E., Piters, A. J. M., Puentedura, O., Richter, A., Schönhardt, A., Shaiganfar, R., Spinei, E., Strong, K., Takashima, H., Vrekoussis, M., Wagner, T., Wittrock, F., and Yilmaz, S.: MAX-DOAS formaldehyde slant column measurements during CINDI: intercomparison and analysis improvement, Atmos. Meas. Tech., 6, 167-185, doi:10.5194/amt-6-167-2013, 2013.

Platt, U. and Stutz, J.: Differential Optical Absorption Spectroscopy. Springer, Heidelberg, Berlin, 229-375, 2008.

Qi, H., Lin, W., Xu, X., Yu, X., and Ma, Q.: Significant downward trend of SO2 observed from 2005 to 2010 at a background station in the Yangtze Delta region, China. Science China Chemistry, 55(7), 1451-1458, 2012.

Qin, M., Xie, P. H., Liu, W. Q., Li, A., Dou, K., Fang, W., Liu, J. G. Zhang, W. J.: Observation of atmospheric nitrous acid with DOAS in Beijing, China, Journal of Environmental Sciences, 18, 69-75, 2006.

Richter, A., Burrows, J. P., Nüß, H., Granier, C., and Niemeier, U.: Increase in tropospheric nitrogen dioxide over China observed from space. Nature, 437(7055), 129-132, 2005

Rodgers, C. D.: Inverse methods for atmospheric sounding, theory and practice, Series on Atmospheric, Oceanic and Planetary Physics, World Scientific, 2000.

Roscoe, H. K., Van Roozendael, M., Fayt, C., du Piesanie, A., Abuhassan, N., Adams, C., Akrami, M., Cede, A., Chong, J., Clémer, K., Friess, U., Gil Ojeda, M., Goutail, F., Graves, R., Griesfeller, A., Grossmann, K., Hemerijckx, G., Hendrick, F., Herman, J., Hermans, C., Irie, H., Johnston, P. V., Kanaya, Y., Kreher, K., Leigh, R., Merlaud, A., Mount, G. H., Navarro, M., Oetjen, H., Pazmino, A., Perez-Camacho, M., Peters, E., Pinardi, G., Puentedura, O., Richter, A., Schönhardt, A., Shaiganfar, R., Spinei, E., Strong, K., Takashima, H., Vlemmix, T., Vrekoussis, M., Wagner, T., Wittrock, F., Yela, M., Yilmaz, S., Boersma, F., Hains, J., Kroon, M., Piters, A., and Kim, Y. J.: Intercomparison of slant column measurements of NO2 and O4 by MAX-DOAS and zenith-sky UV and visible spectrometers, Atmos. Meas. Tech., 3, 1629-1646, doi:10.5194/amt-3-1629-2010, 2010.

Rozanov, A., Rozanov, V., Buchwitz, M., Kokhanovsky, A., and Burrows, J.: SCIATRAN 2.0 - A new radiative transfer model for geophysical applications in the 175-2400 nm spectral region, in: Atmospheric Remote Sensing: Earth's Surface, Troposphere, Stratosphere and Mesosphere - I, edited by Burrows, J. and Eichmann, K., vol. 36 of ADVANCES IN SPACE RESEARCH, 1015-1019, 2005.

Schaub, D., Brunner, D., Boersma, K. F., Keller, J., Folini, D., Buchmann, B., Berresheim, H., and Staehelin, J.: SCIAMACHY tropospheric NO2 over Switzerland: estimates of NOx lifetimes and impact of the complex Alpine topography on the retrieval, Atmos. Chem. Phys., 7, 5971-5987, doi: 10.5194/acp-7-5971-2007, 2007.

Seinfeld, J. H. and Pandis, S. N.: Atmospheric Chemistry and Physics — From Air Pollution to Climate Change. John Wiley, New York, 1998.

Shaiganfar, R., Beirle, S., Sharma, M., Chauhan, A., Singh, R. P., and Wagner, T.: Estimation of NO$_x$ emissions from Delhi using Car MAX-DOAS observations and comparison with OMI satellite data, Atmos. Chem. Phys., 11, 10871-10887, doi:10.5194/acp-11-10871-2011, 2011.

Sinreich, R., Merten, A., Molina, L., and Volkamer, R.: Parameterizing radiative transfer to convert MAX-DOAS dSCDs into near-surface box averaged mixing ratios and vertical profiles, Atmos. Meas. Tech., 6, 1521-1532, 2013.

Smirnov, A., Holben, B. N., Eck, T. F., Dubovik, O. and Slutsker, I.: Cloud-Screening and Quality Control Algorithms for the AERONET Database, Remote Sensing of Environment, 73, 337, 2000.

Stavrakou, T., Müller, J.-F., Boersma, K. F., van der A, R. J., Kurokawa, J., Ohara, T., and Zhang, Q.: Key chemical NOx sink uncertainties and how they influence top-down emissions of nitrogen oxides, Atmos. Chem. Phys., 13, 9057–9082, doi:10.5194/acp-13-9057-2013, 2013.

Theys, N., De Smedt, I., Gent, J., Danckaert, T., Wang, T., Hendrick, F., Stavrakou, T., Bauduin, S., Clarisse, L., Li, C., Krotkov, N., Yu, H., Brenot, H., and Van Roozendael, M.: Sulfur dioxide vertical column DOAS retrievals from the Ozone Monitoring Instrument: Global observations and comparison to ground‐based and satellite data. Journal of Geophysical Research: Atmospheres, 120(6), 2470-2491, 2015.

Vandaele, A. C., Hermans, C., Simon, P. C., Carleer, M., Colin, R., Fally, S., Mérienne, M.-F., Jenouvrier, A., and Coquart, B.: Measurements of the NO2 absorption cross section from 42000 cm^{-1} to 10000 cm^{-1} (238–1000 nm) at 220 K and 294 K, J. Quant. Spectrosc. Ra., 59, 171–184, 1998.

Van Roozendael, M., Fayt, C., Post, P., Hermans, C., Lambert, J.-C.: Retrieval of BrO and NO2 from UV-Visible Observations, in: Sounding the troposphere from space: a new Era for Atmospheric Chemistry. The TROPOSAT Final Report. Peter Borrell, Patricia M. Borrell, John P. Burrows and Ulrich Platt (editors), Springer, 155-166, 2003

Veefkind, J. P., Boersma, K. F., Wang, J., Kurosu, T. P., Krotkov, N., Chance, K., and Levelt, P. F.: Global satellite analysis of the relation between aerosols and short-lived trace gases, Atmos. Chem. Phys., 11, 1255–1267, doi:10.5194/acp-11-1255-2011, 2011.

Vlemmix, T., Eskes, H. J., Piters, A. J. M., Schaap, M., Sauter, F. J., Kelder, H., and Levelt, P. F.: MAX-DOAS tropospheric nitrogen dioxide column measurements compared with the Lotos-Euros air quality model, Atmos. Chem. Phys., 15, 1313-1330, doi:10.5194/acp-15-1313-2015, 2015a.

Vlemmix, T., Hendrick, F., Pinardi, G., De Smedt, I., Fayt, C., Hermans, C., Piters, A., Wang, P., Levelt, P., and Van Roozendael, M.: MAX-DOAS observations of aerosols, formaldehyde and nitrogen dioxide in the Beijing area: comparison of two profile retrieval approaches, Atmos. Meas. Tech., 8, 941-963, doi:10.5194/amt-8-941-2015, 2015b.

Vlemmix, T., Piters, A. J. M., Berkhout, A. J. C., Gast, L. F. L., Wang, P., and Levelt, P. F.: Ability of the MAX-DOAS method to derive profile information for NO2: can the boundary layer and free troposphere be separated?, Atmos. Meas. Tech., 4, 2659–2684, 2011

Vlemmix, T., Piters, A. J. M., Stammes, P., Wang, P., and Levelt, P. F.: Retrieval of tropospheric NO_2 using the MAX-DOAS method combined with relative intensity measurements for aerosol correction, Atmos. Meas. Tech., 3, 1287–1305, 2010.

Von Glasow, R., Bobrowski, N., and Kern, C.: The effects of volcanic eruptions on atmospheric chemistry, Chem. Geol., 263, 131–142, doi:10.1016/j.chemgeo.2008.08.020, 2009.

Wagner, T., Erie, F., Marquard, L., Otten, C., Pfeilsticker, K., Senne, T., Stutz, J. and Platt, U.: Cloudy sky optical paths as derived from differential optical absorption spectroscopy observations, J. Geophys. Res., 103, 25307, 1998.

Wagner, T., Friedeburg, C. von, Wenig M., Otten, C. and Platt, U.: UV/vis observations of atmospheric O4 absorptions using direct moon light and zenith scattered sunlight under clear and cloudy sky conditions, J. Geophys. Res., 107, D204424, 2002.

Wagner, T., B. Dix, C. von Friedeburg, Frieß, U., Sanghavi, S., Sinreich, R. and Platt, U.: MAX-DOAS O_4 measurements: A new technique to derive information on atmospheric aerosols—Principles and information content, J. Geophys. Res., 109, D22205, 2004.

Wagner, T., Beirle, S., and Deutschmann, T.: Three-dimensional simulation of the Ring effect in observations of scattered sun light using Monte Carlo radiative transfer models, Atmos. Meas. Tech., 2, 113-124, 2009.

Wagner, T., Beirle, S., Brauers, T., Deutschmann, T., Frieß, U., Hak, C., Halla, J. D., Heue, K. P., Junkermann, W., Li, X., Platt, U. and Pundt-Gruber, I.: Inversion of tropospheric profiles of aerosol extinction and HCHO and NO_2 mixing ratios from MAX-DOAS observations in Milano during the summer of 2003 and comparison with independent data sets, Atmos. Meas. Tech. Discuss, 4, 3891–3964, 2011.

Wagner, T., Beirle, S., Dörner, S., Friess, U., Remmers, J. and Shaiganfar, R.: Cloud detection and classification based on MAX-DOAS observations, Atmos. Meas. Tech., 7, 1289-1320, 2014

Wang, T., Nie, W., Gao, J., Xue, L. K., Gao, X. M., Wang, X. F., Qiu, J., Poon, C. N., Meinardi, S., Blake, D., Wang, S. L., Ding, A. J., Chai, F. H., Zhang, Q. Z., and Wang, W. X.: Air quality during the 2008 Beijing Olympics: secondary pollutants and regional impact, Atmos. Chem. Phys., 10, 7603-7615, doi:10.5194/acp-10-7603-2010, 2010.

Wang, T., Hendrick, F., Wang, P., Tang, G., Clémer, K., Yu, H., Fayt, C., Hermans, C., Gielen, C., Müller, J.-F., Pinardi, G., Theys, N., Brenot, H., and Van Roozendael, M.: Evaluation of tropospheric SO_2 retrieved from MAX-DOAS measurements in Xianghe, China, Atmos. Chem. Phys., 14, 11149-11164, doi:10.5194/acp-14-11149-2014, 2014a.

Wang, Y., Li, A., Xie, P. H., Chen, H., Xu, J., Wu, F. C., G., L. J., and Q., L. W.: Retrieving vertical profile of aerosol extinction by multi-axis differential optical absorption spectroscopy, Acta Phys. Sin., 16, doi: 10.7498/aps.62.180705, http://wulixb.iphy.ac.cn/EN/abstract/abstract54703.shtml#, 2013a.

Wang, Y., Li, A., Xie, P. H., Chen, H., Mou, F. S., Xu, J., Wu, F. C., Zeng, Y., Liu, J. G. and Liu, W. Q.: Measuring tropospheric vertical distribution and vertical column density of NO2 by multi-axis differential optical absorption spectroscopy, Acta Phys. Sin., 16, DOI:10.7498/aps.62.200705, http://wulixb.iphy.ac.cn/EN/abstract/abstract56201.shtml, 2013b.

Wang, Y., Li, A., Xie, P. H., Wagner, T., Chen, H., Liu, W. Q., and Liu, J. G.: A rapid method to derive horizontal distributions of trace gases and aerosols near the surface using multi-axis differential optical absorption spectroscopy, Atmos. Meas. Tech., 7, 1663-1680, doi:10.5194/amt-7-1663-2014, 2014b.

Wang, Y., Penning de Vries, M., Xie, P. H., Beirle, S., Dörner, S., Remmers, J., Li, A., and Wagner, T.: Cloud and aerosol classification for 2.5 years of MAX-DOAS observations in Wuxi (China) and comparison to independent data sets, Atmos. Meas. Tech., 8, 5133-5156, doi:10.5194/amt-8-5133-2015, 2015.

Winterrath, T., Koruso, T. P., Richter, A. and Burrows, J. P.: Enhanced O_3 and NO_2 in thunderstorm clouds: convection or production, *Geophys. Res. Lett.*, 26, 1291, 1999.

Wittrock, F., Oetjen, H., Richter, A., Fietkau, S., Medeke, T., Rozanov, A., and Burrows, J. P.: MAX-DOAS measurements of atmospheric trace gases in Ny-Alesund – Radiative transfer studies and their application, Atmos. Chem. Phys., 4, 955–966, 2004.

Wittrock, F.: The Retrieval of Oxygenated Volatile Organic Compounds by Remote Sensing Techniques. Ph.D., University of Bremen, Bremen, Germany, 2006, Available at: http://www.doas-bremen.de/paper/diss_wittrock_06.pdf (last accessed December 2015).

Xie, X., Shao, M., Liu, Y., Lu, S., Chang, C. C., and Chen, Z. M.: Estimate of initial isoprene contribution to ozone formation potential in Beijing, China. Atmospheric Environment, 42(24), 6000-6010, 2008.

Xue, L., Ding, A., Gao, J., Wang, T., Wang, W., Wang, X., Lei, H., Jin, D., and Qi, Y.: Aircraft measurements of the vertical distribution of sulfur dioxide and aerosol scattering coefficient in China. Atmospheric Environment, 44(2), 278-282, 2010.

Yilmaz, S.: Retrieval of Atmospheric Aerosol and Trace Gas Vertical Profiles using Multi-Axis Differential Optical Absorption Spectroscopy, PhD thesis, University of Heidelberg, Germany, 2012.

Thalman, R. M. and Volkamer, R.: Temperature Dependent Absorption Cross-Sections of O2-O2 collision pairs between 340 and 630 nm and at atmospherically relevant pressure, Phys. Chem. Chem. Phys., 15, 15371–15381, doi:10.1039/c3cp50968k, 2013

Figures

(a)

(b)

(c)

(d)
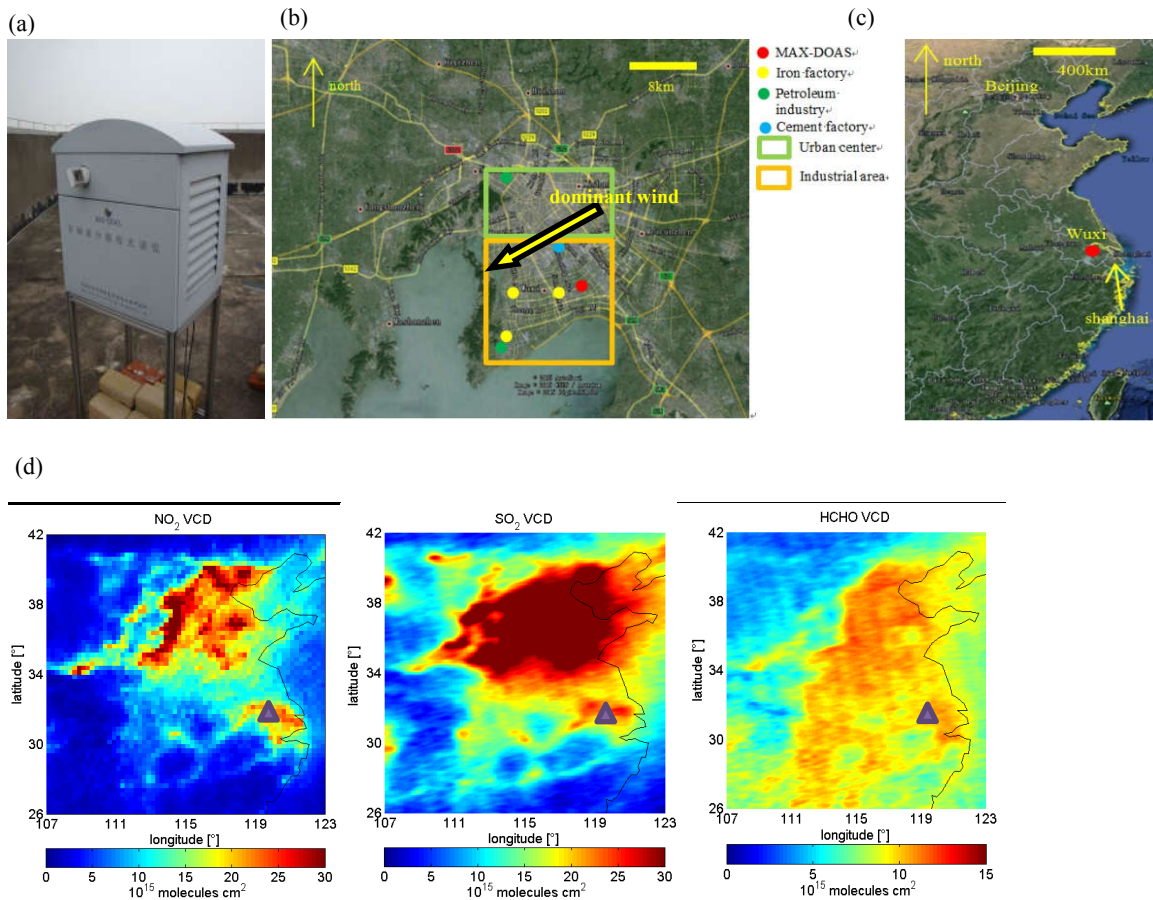
Figure 1: The MAX-DOAS instrument (a) (also the long path DOAS and the visibility meter) is operated at the location marked by the red dot in subfigure (b) in Wuxi city (c). In subfigure (b), the dots with different colours indicate the positions of different types of emission sources; the green and orange blocks indicate the urban centre and industrial area, respectively; the yellow arrow represents the dominant wind direction (north-easterly wind). The maps of mean tropospheric VCDs of NO₂ (from DOMINO version 2), SO₂ (from BIRA, Theys et al., 2015) and HCHO (from BIRA, I. De Smedt et al., 2015) derived from OMI observations over eastern China in the period from 2011 to 2014 are shown in subfigure (d), in which the triangles indicate the location of Wuxi.
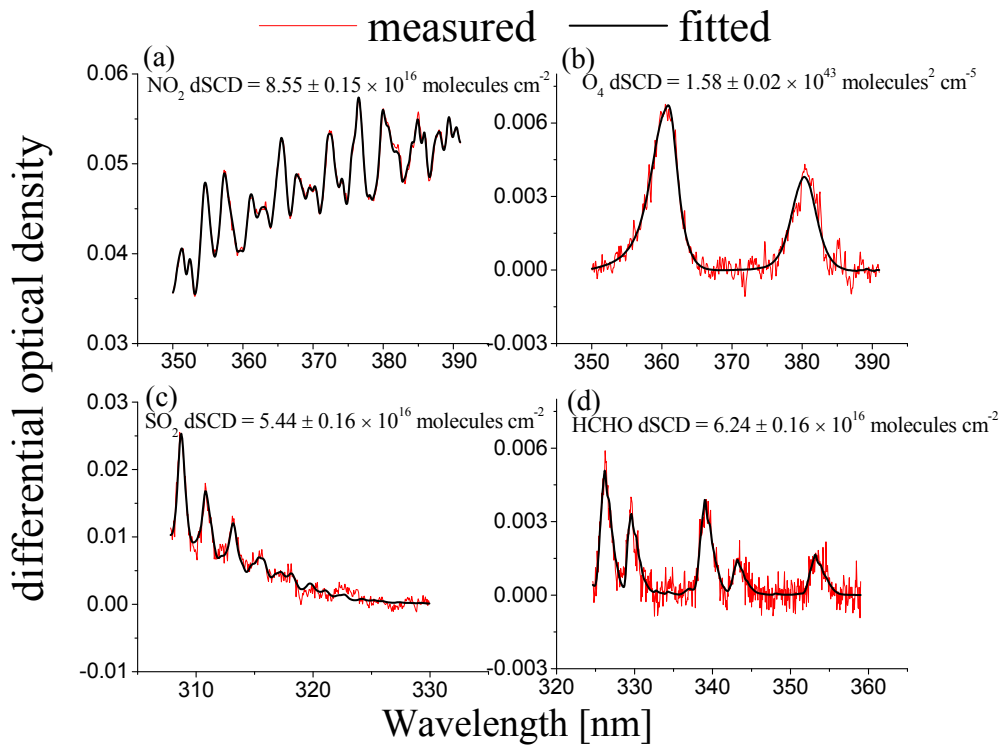
Figure 2: Examples of typical DOAS fits of NO₂ (a), O₄ (b) and SO₂ (c) at 11:37 on 1 December 2011 as well as HCHO (d) at 11:34 on 12 July 2012. The fitted dSCDs of NO₂, O₄, SO₂ and HCHO are given in the corresponding subfigures. The black and red curves indicate the fitted absorption structures and the derived absorption structures from the measured spectra, respectively.
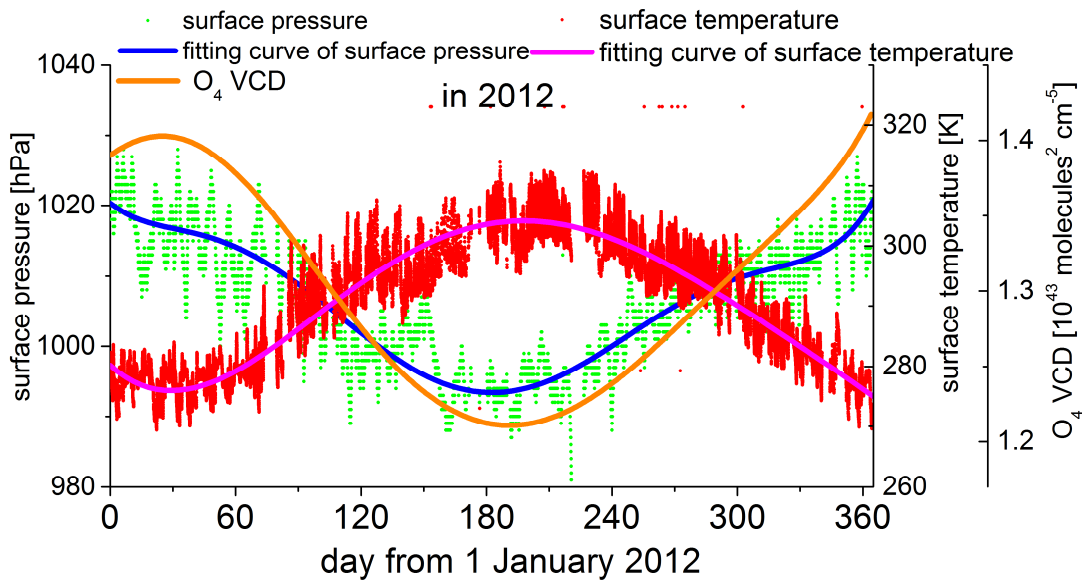
Figure 3: Annual variation of surface temperature, surface pressure as well as fitted 6ᵗʰ order polynomials in 2012. Also the O₄ VCDs calculated based on the fitted curves of the measured annual variations of surface temperature and pressure in 2012 is shown (similar results are found for other years).
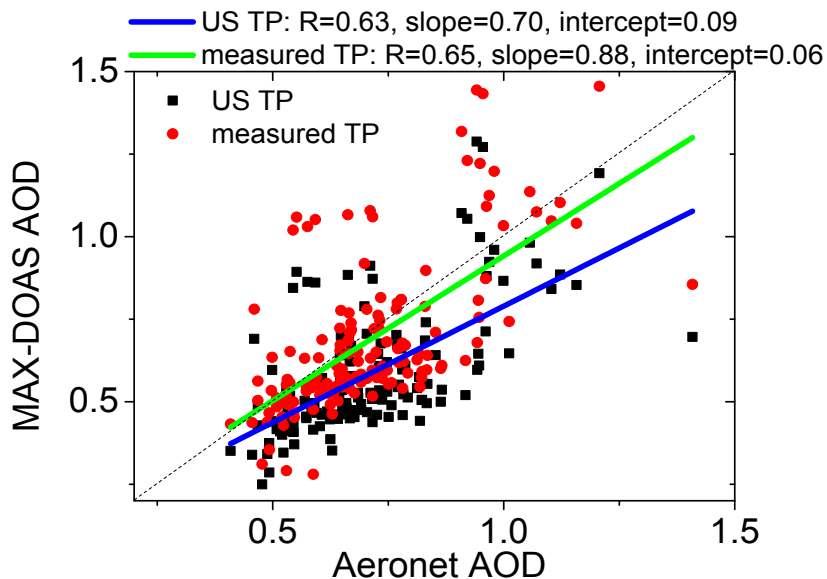
Figure 4: AODs retrieved from MAX-DOAS observations (using either the US standard summer TP profile or the explicit TP from measurements) plotted against those from the Taihu AERONET station for clear sky conditions. The results of the linear regressions are shown on top of the diagram.
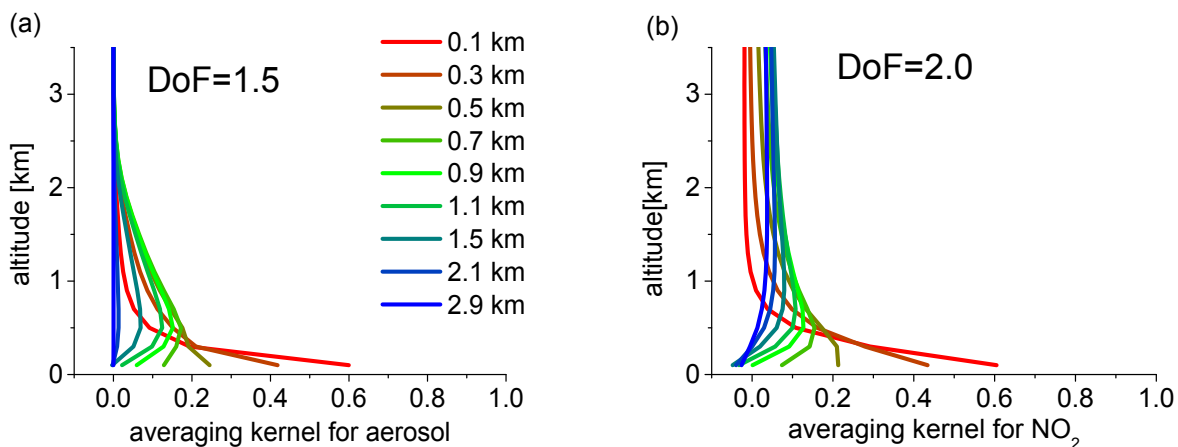
Figure 5: a totally averaged averaging kernel of aerosol (a) and NO$_2$ (b) retrievals for all the MAX-DOAS measurements for clear sky conditions with low aerosol loading. DoF is the degrees of freedom related to the averaging kernel.
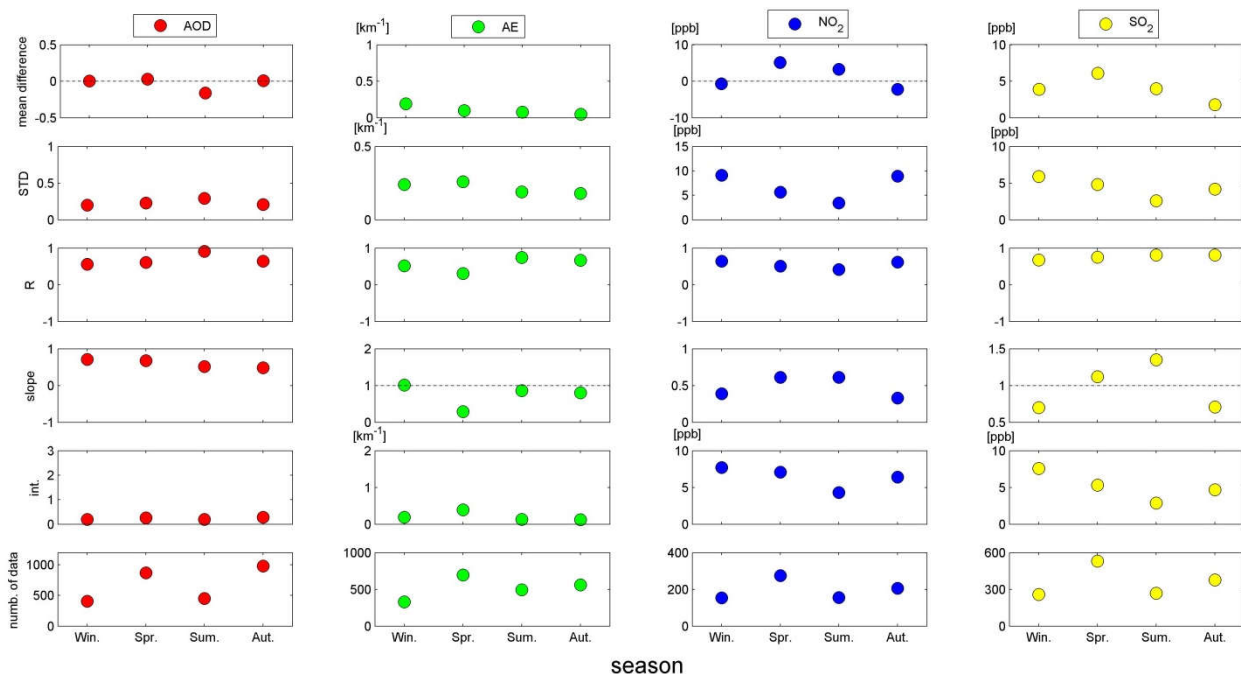
Figure 6: Mean absolute differences, standard deviations as well as correlation coefficients (R), slopes and intercepts derived from linear regressions of the AODs, near-surface AE, NO_2 and SO_2 VMRs between MAX-DOAS and independent techniques for different seasons for clear sky conditions with low aerosol loads. The corresponding number of data points is shown in the bottom panel. Different colours denote AOD (compared with the Taihu AERONET level 1.5 data sets), AE (compared with the nearby visibility meter) and NO_2 and SO_2 (compared with the nearby long path DOAS instrument). For calculations of mean absolute differences, the data derived from independent techniques are subtracted from those derived from the MAX-DOAS instrument. The data derived from the MAX-DOAS instrument are plotted against those derived from independent techniques for linear regressions.

Figure 7: Histograms of the differences between the measured and modelled dSCDs of O_4 (a), NO_2 (b), SO_2 (c) and HCHO (d) for
all elevation angles. The colour bars show the relative frequencies of the different sky conditions for each bin (top). The grey
hollow bars (bottom) represent the relative frequencies of the number of measurements compared to the total number of
observations.
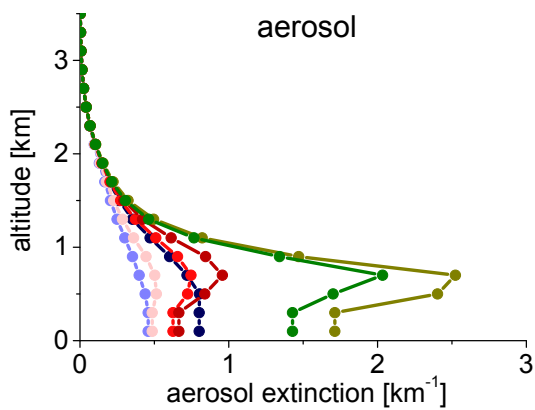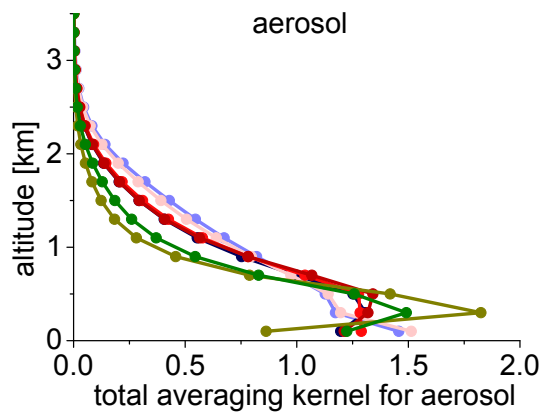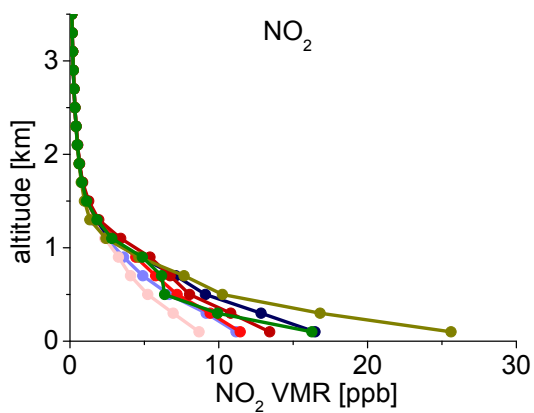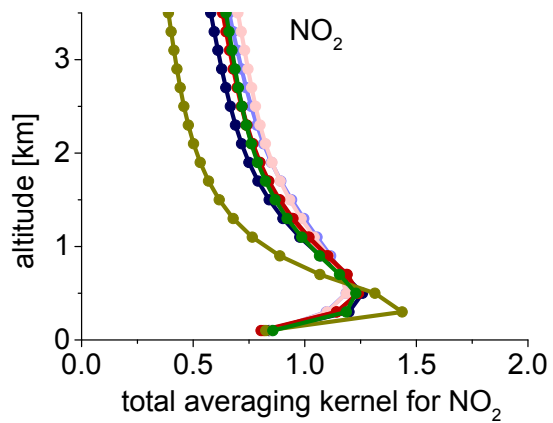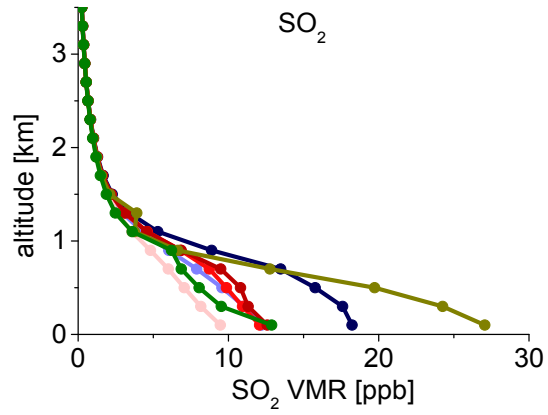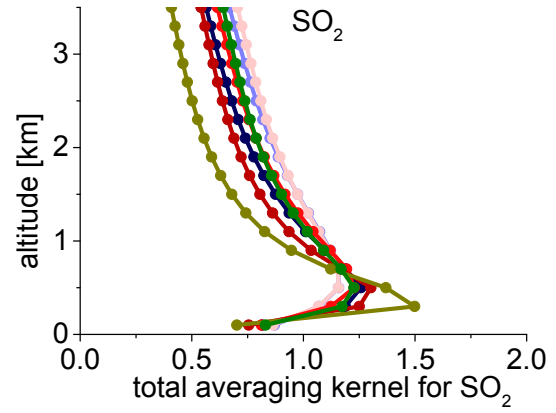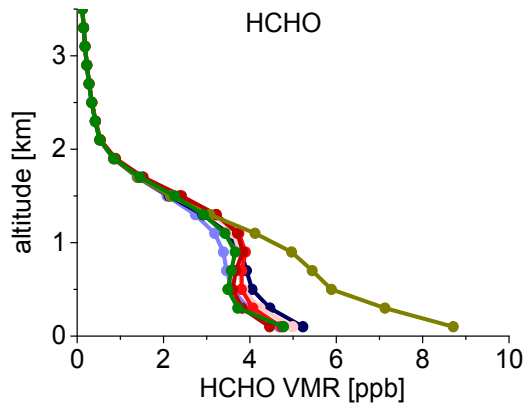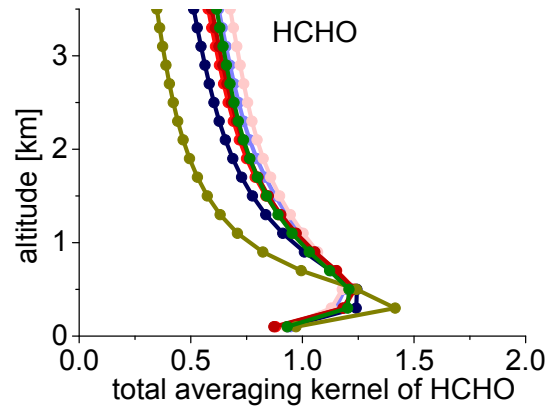
5 **Figure 8: Mean profiles of aerosol extinctions (a), NO₂ VMRs (c), SO₂ VMRs (e) and HCHO VMRs (g) from all MAX-DOAS observations under individual sky conditions; the subfigures (b), (d), (f), (h) show the total averaging kernels of the four species under individual sky conditions.**
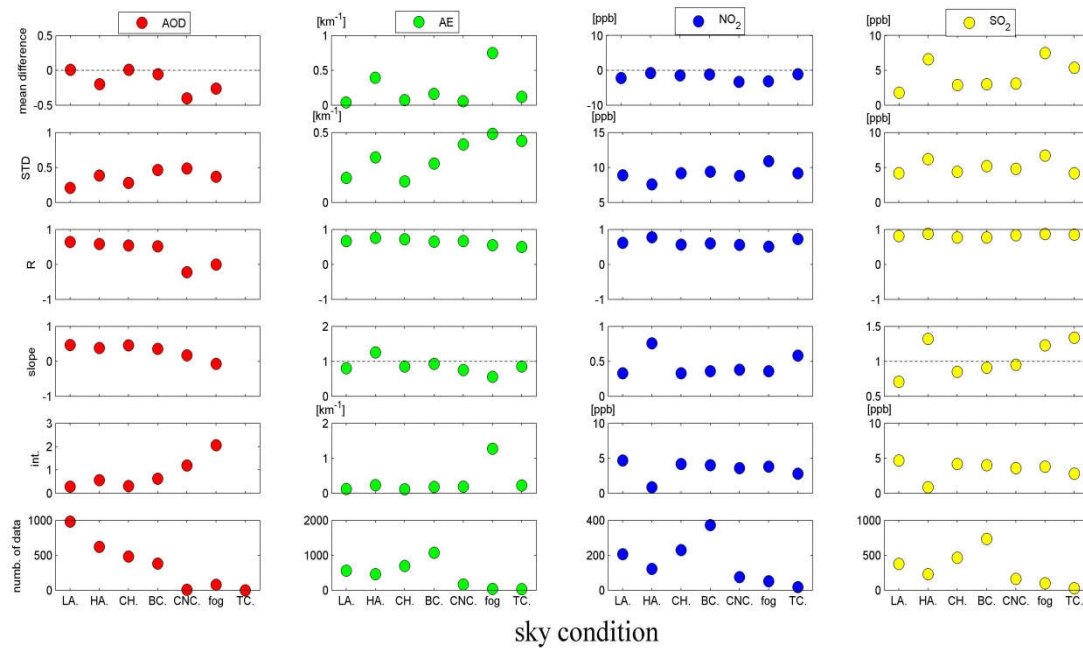
Figure 9: Mean absolute differences, standard deviations as well as correlation coefficients (R), slopes and intercepts derived from linear regressions of the AODs, near-surface AE, NO₂ and SO₂ VMRs between MAX-DOAS and independent techniques for different sky conditions in autumn. The corresponding number of data points is shown in the bottom panel. Different colours denote AOD (compared with the Taihu AERONET level 1.5 data sets), AE (compared with the nearby visibility meter) and NO₂ and SO₂ (compared with the nearby long path DOAS instrument). For calculations of mean absolute differences, the data derived from independent techniques are subtracted from those derived from the MAX-DOAS instrument. The data derived from the MAX-DOAS instrument are plotted against those derived from independent techniques for linear regressions.
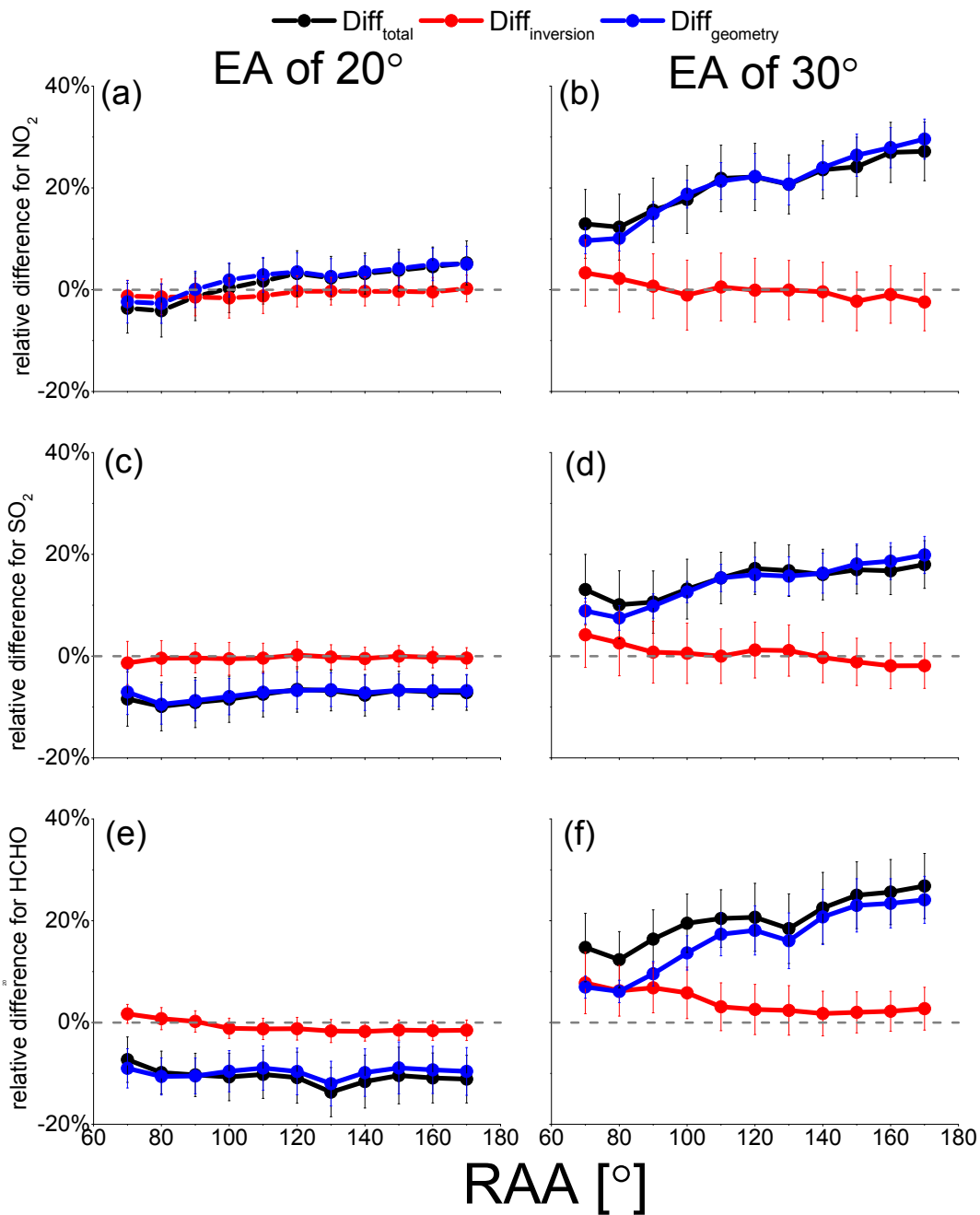
Figure 10: Relative differences of the tropospheric NO_2 (top row), SO_2 (middle row) and HCHO (bottom row) VCDs derived by the geometric approximation and from the profile inversion ($Diff_{total}$, black dots) as function of the relative azimuth angle for elevation angles of 20° (left) and 30° (right). Also the differences caused by the errors of the profile retrieval ($Diff_{inversion}$, red dots) and of the geometric approximation ($Diff_{geometry}$, blue dots) are shown. $Diff_{total}$, $Diff_{inversion}$, and $Diff_{geometry}$ are calculated by Eq. 3, 4, and 5 in the text.
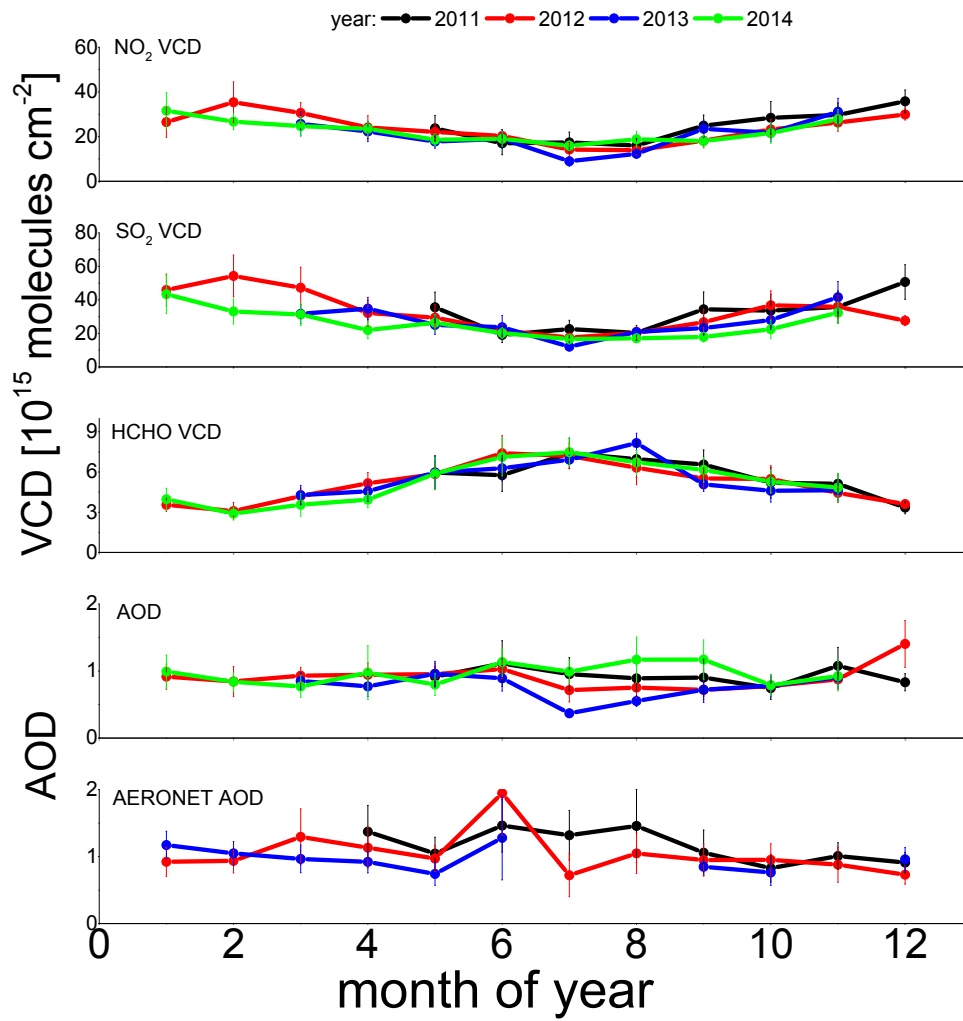
(b)
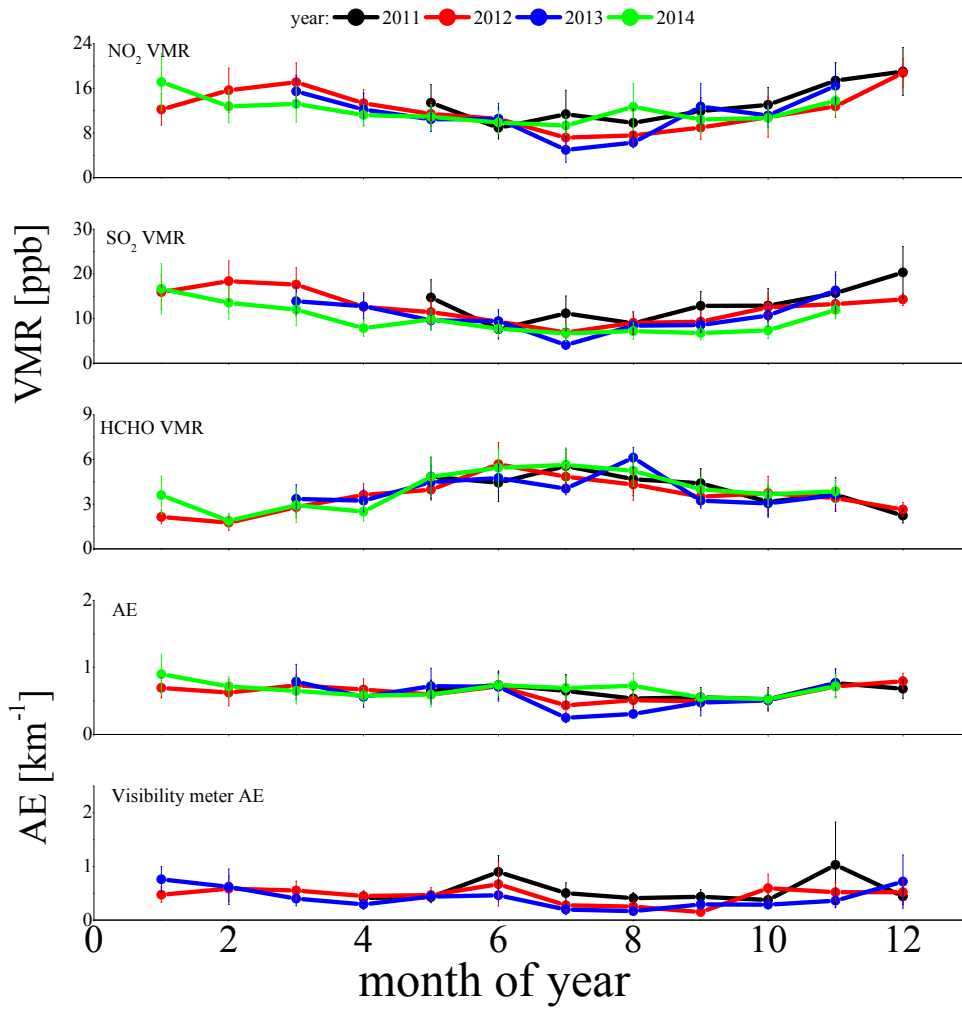
(c)
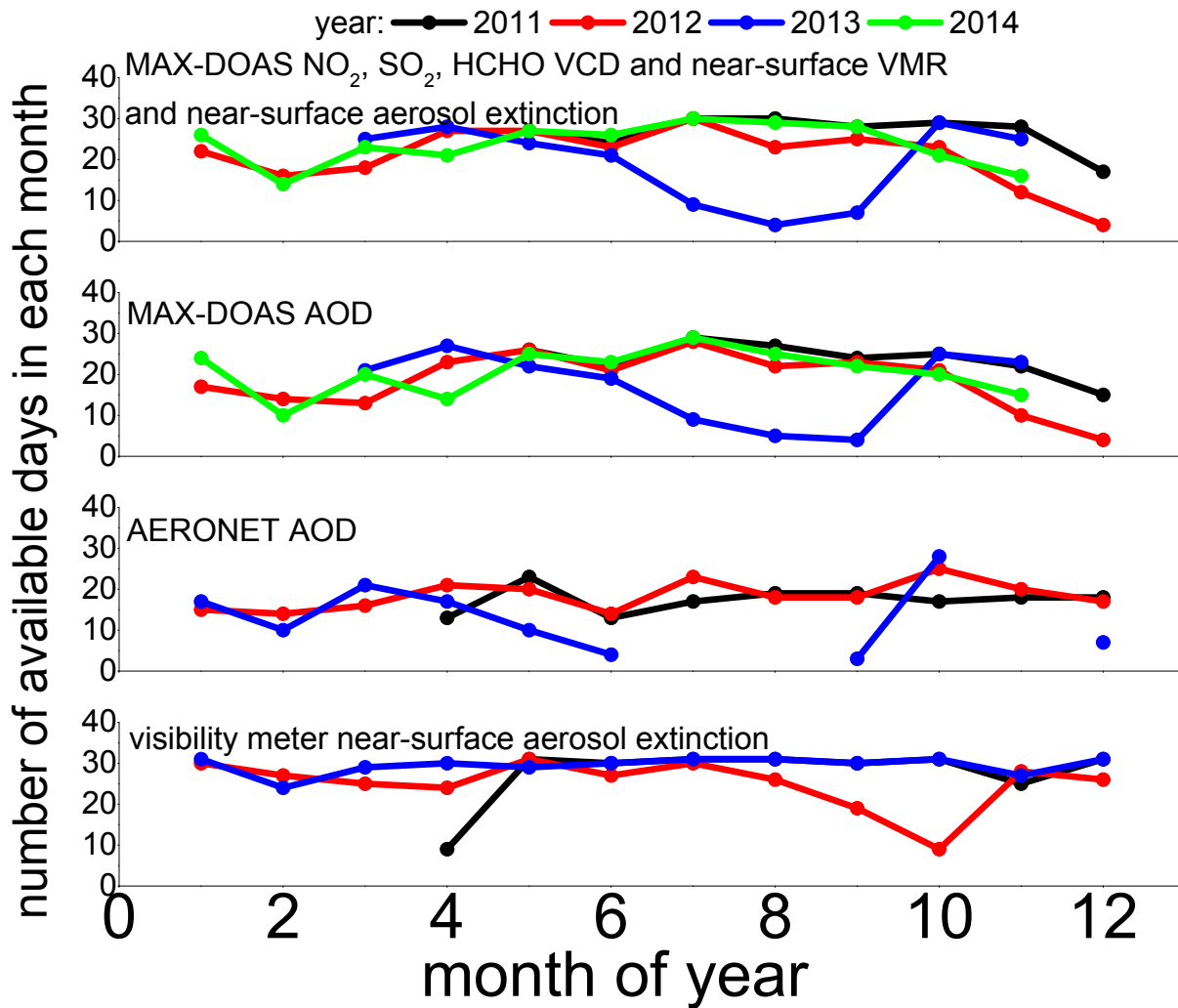
Figure 11: Seasonal cycle of monthly mean MAX-DOAS results: VCD and AOD (a), and near-surface VMR of NO₂, SO₂ and HCHO and AE (b) for May 2011 to November 2014. The error bars represent the standard deviations. In addition to the MAX-DOAS data also AOD and AE from AERONET and visibility meter are shown, respectively. The numbers of available days in each month for MAX-DOAS measurements, AERONET and visibility meter are shown in subfigure (c). The different numbers of available AOD and trace gas data derived from MAX-DOAS are caused by the filtering scheme (see Table 3).
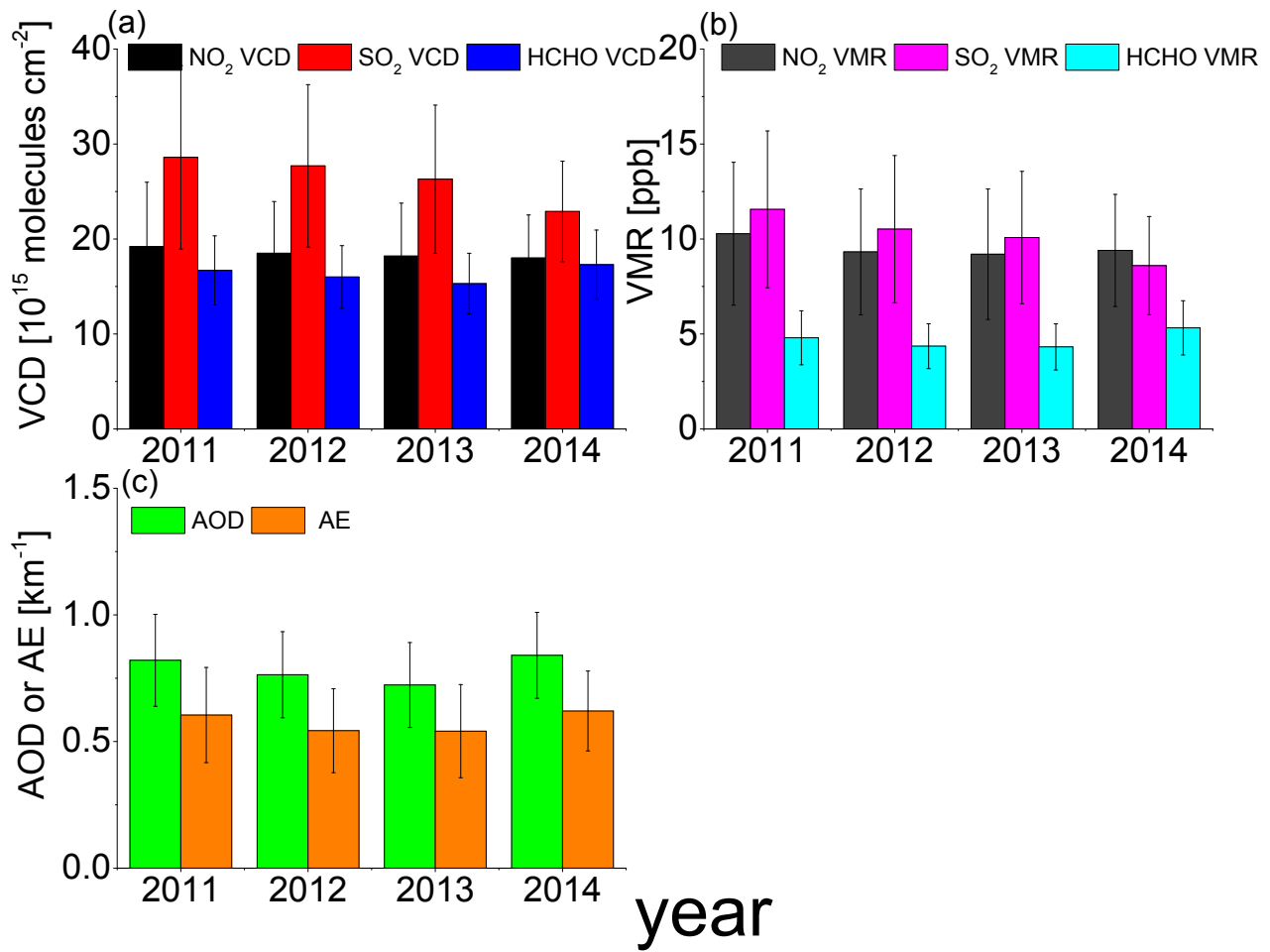
Figure 12: Mean (May to November) VCDs (a) and near surface VMRs (b) of NO₂, SO₂, HCHO as well as AODs and near surface aerosol extinctions (c) for each year.

(c)

HCHO VMR [ppb]

(d)

aerosol extinction [km^{-1}]
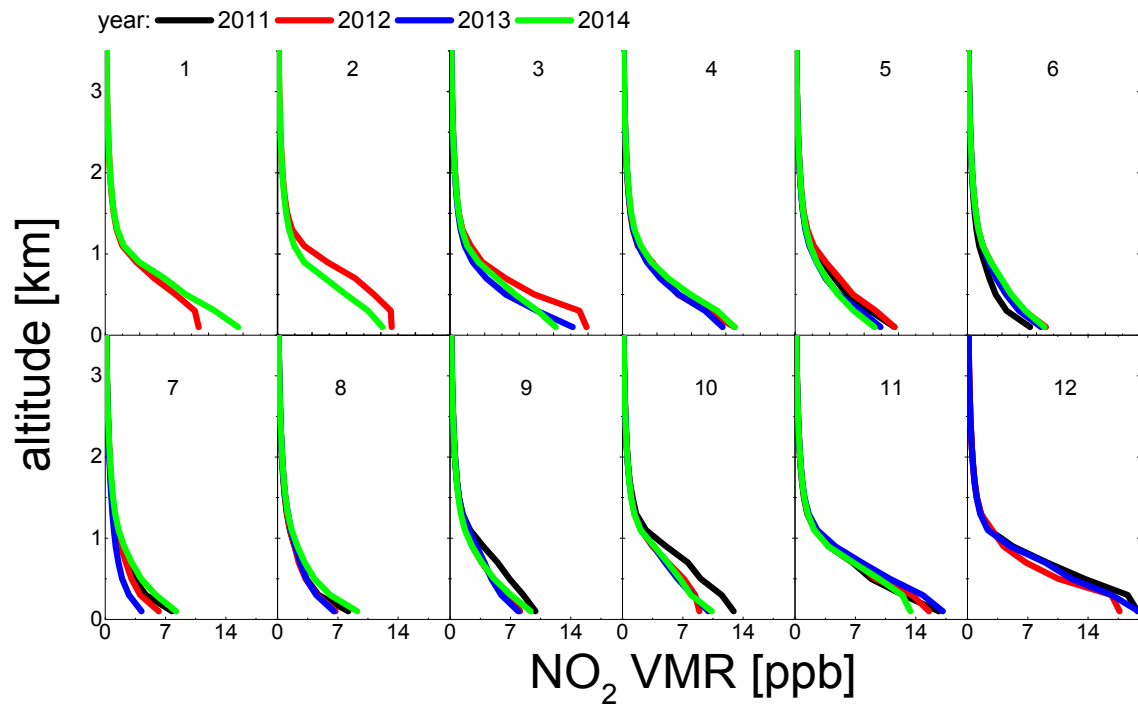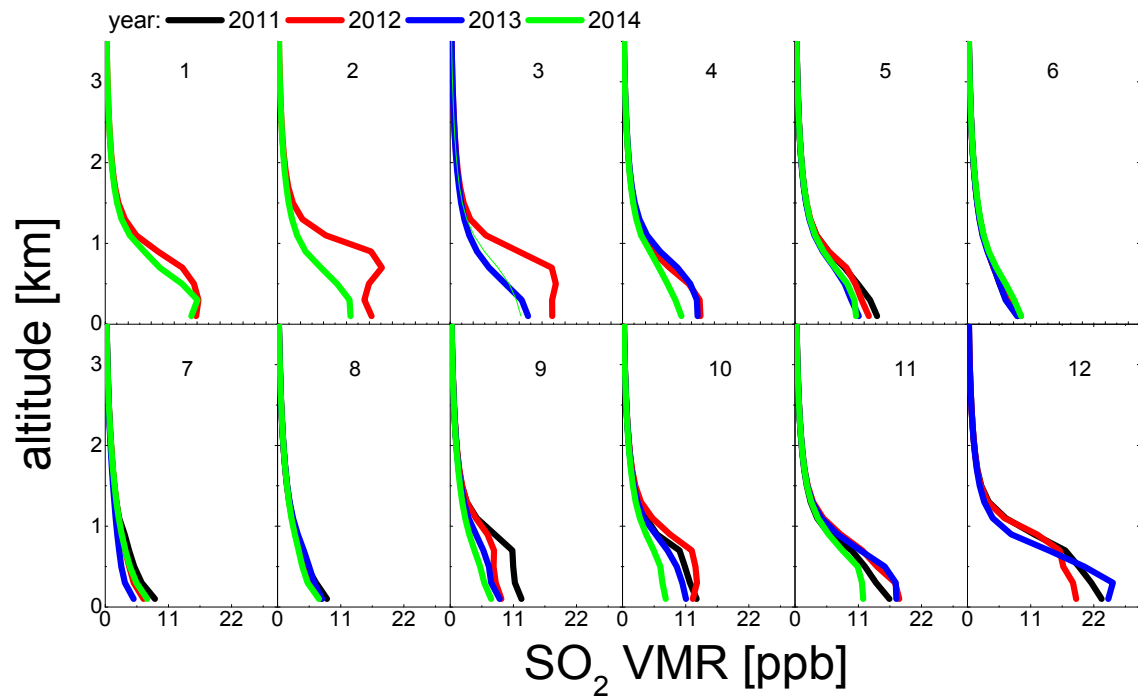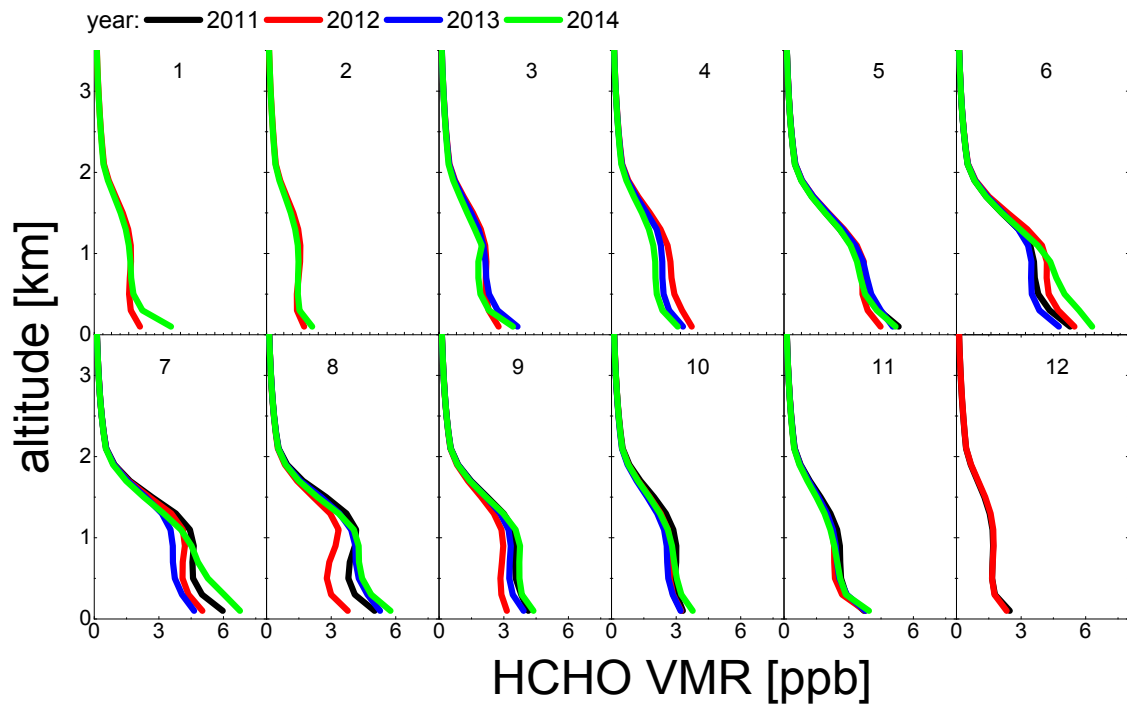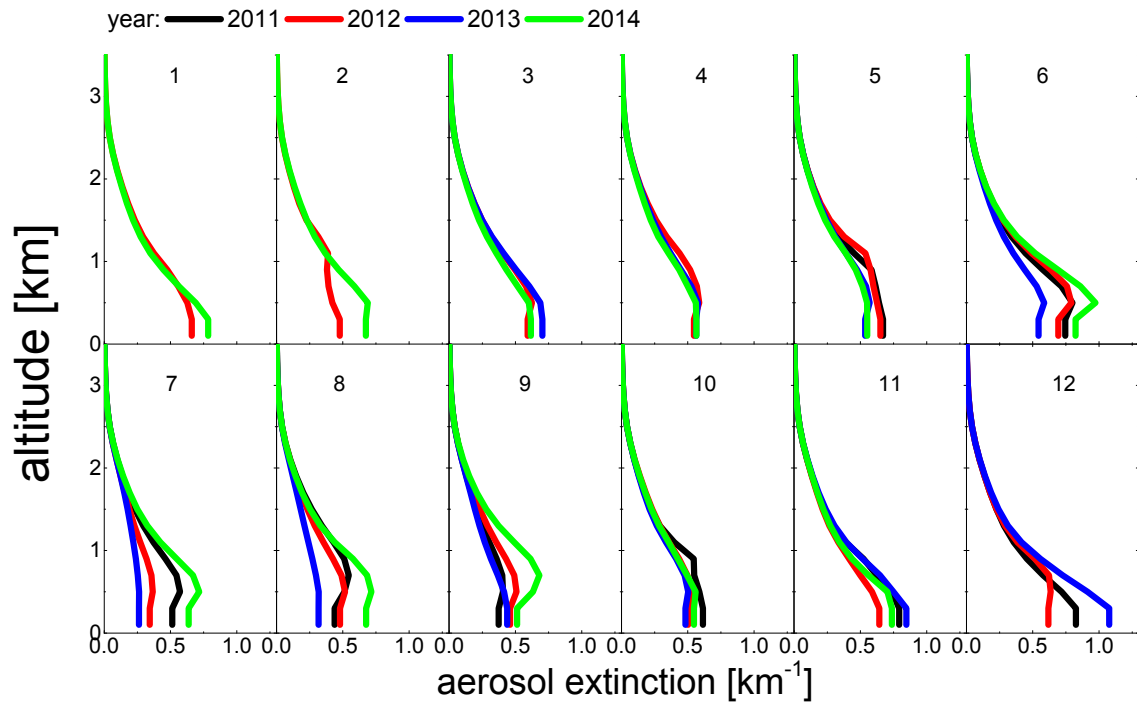
Figure 13: Monthly mean profiles of NO₂ (a), SO₂ (b), HCHO (c) VMRs (under clear and cloudy sky conditions except thick clouds and fog) and aerosol extinction (under clear sky conditions) (d) for the period from May 2011 to November 2014.

(a)

(b)

(c)

(d)
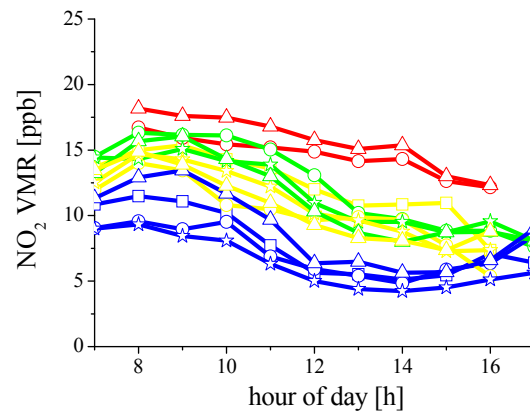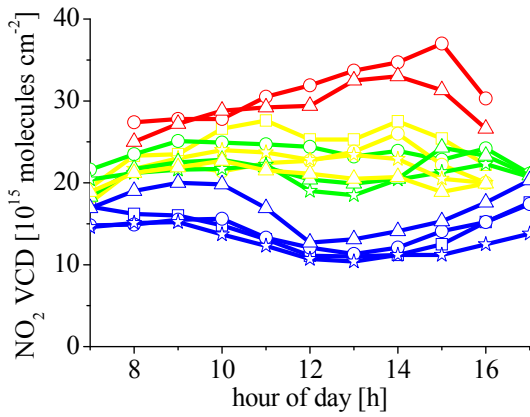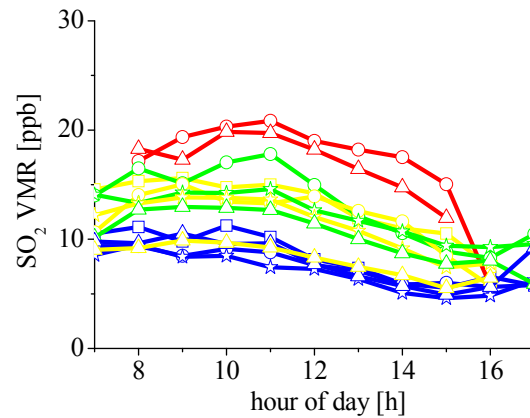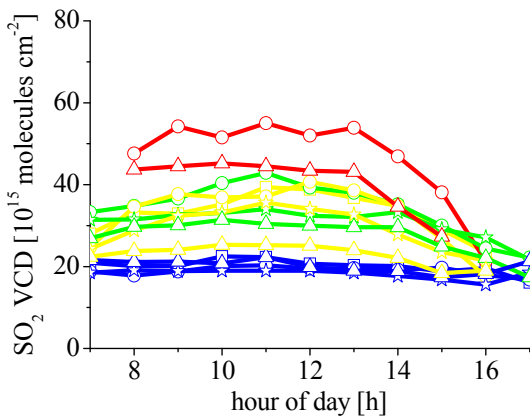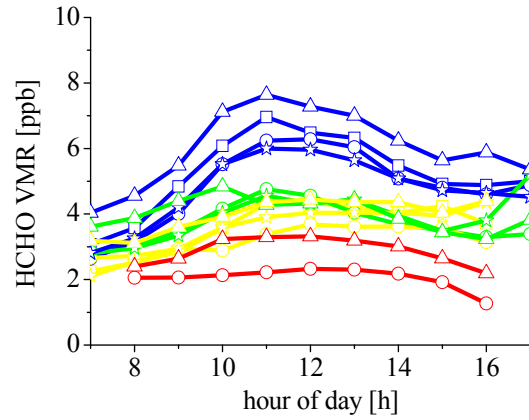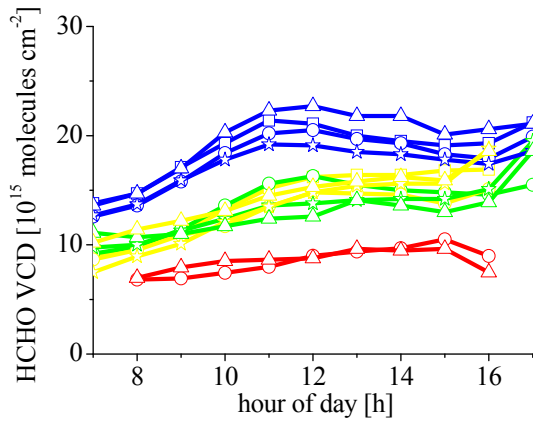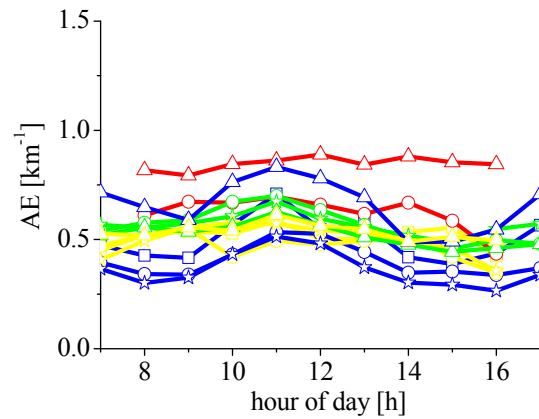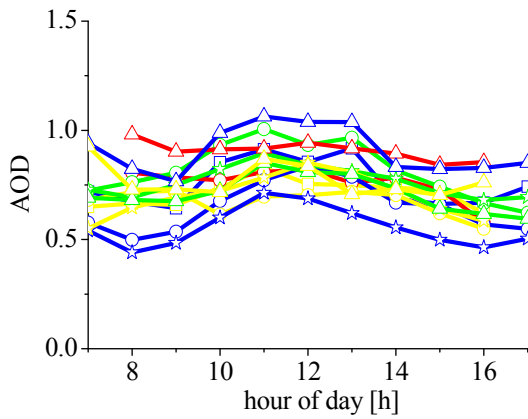
Figure 14: Seasonally averaged diurnal variations of trace gas VCDs and AOD (left) and near surface values (right) of NO$_2$ (a), SO$_2$ (b), HCHO (c) and aerosols (d) from 2011 to 2014.
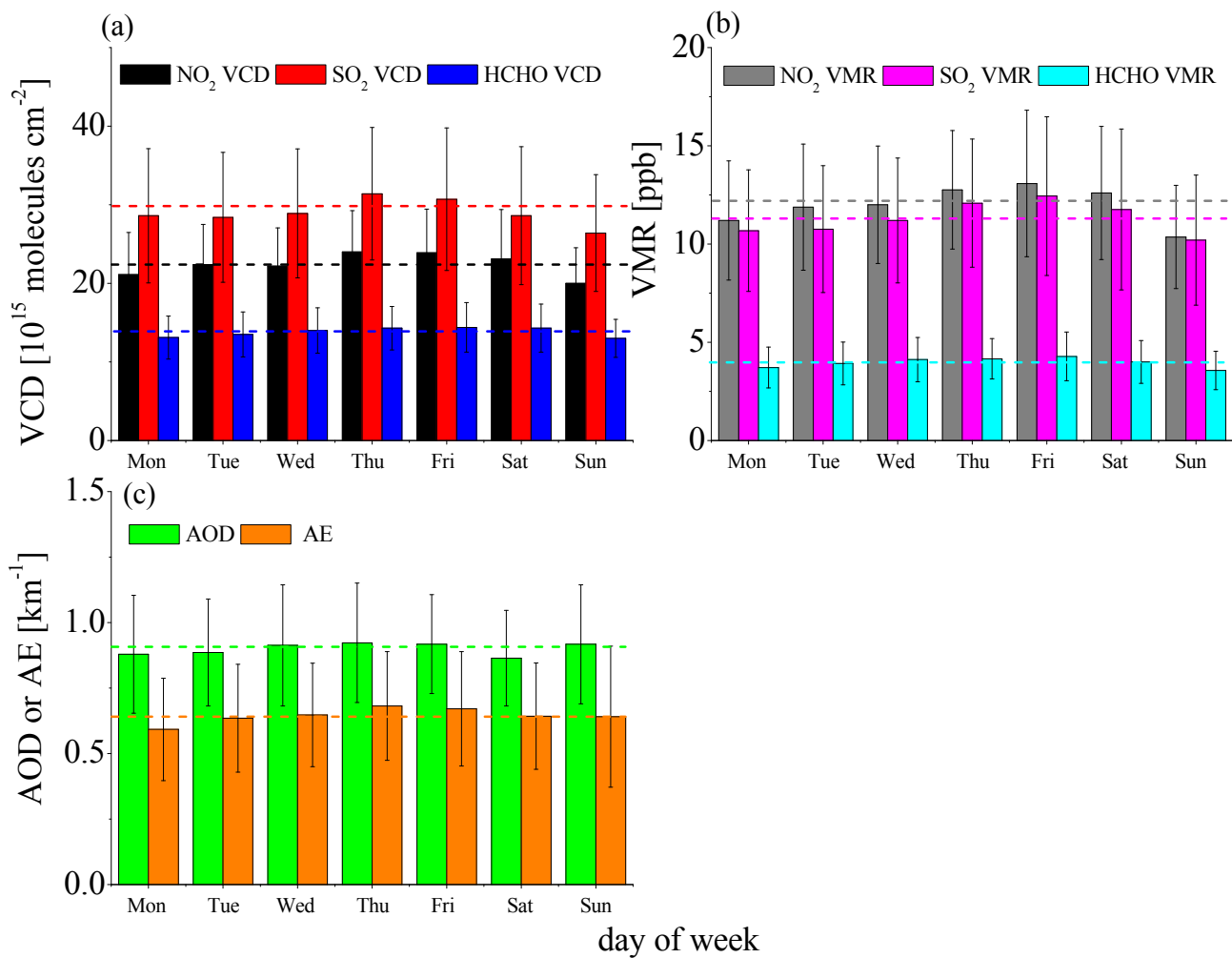
Figure 15: Mean weekly cycles of VCDs (a) and near-surface VMRs (b) of NO₂, SO₂ and HCHO as well as the AODs and near-surface AE (c) for all MAX-DOAS observations from 2011 to 2014. The dashed lines denote the mean values during the working days from Monday to Friday (same colours as for the bars).

(a)

(b)

(c)

(d)
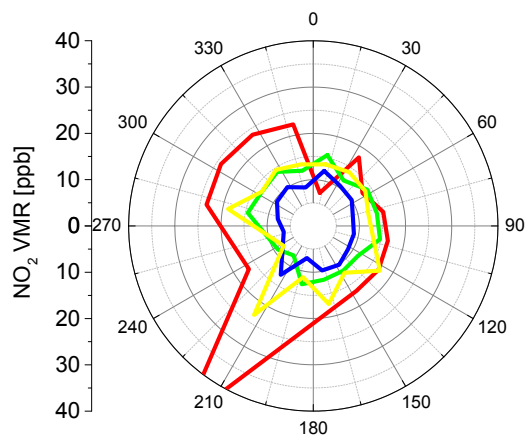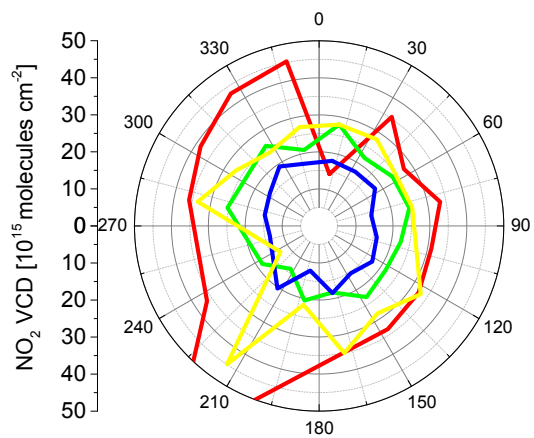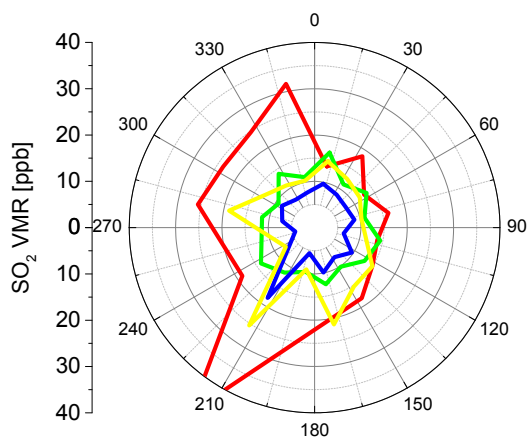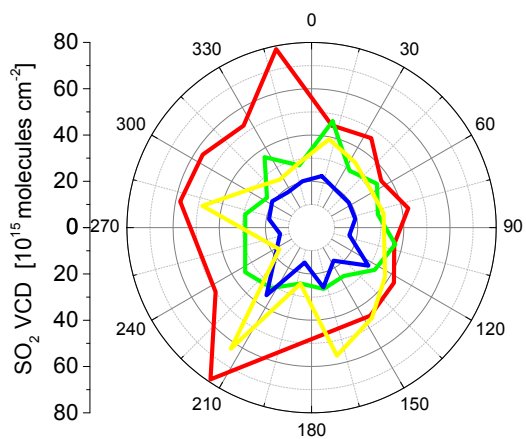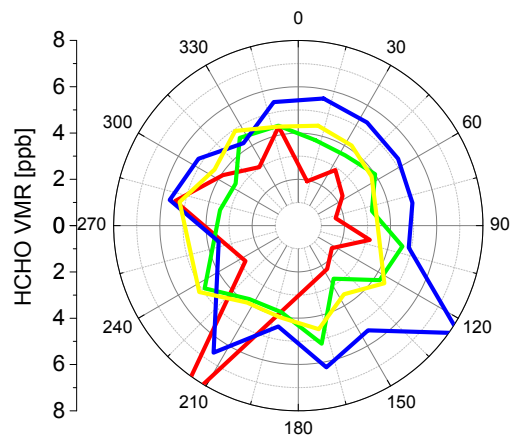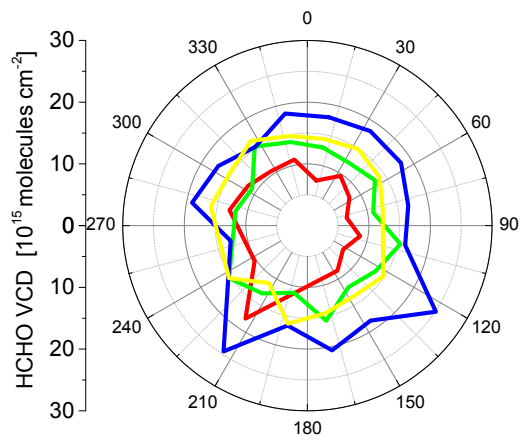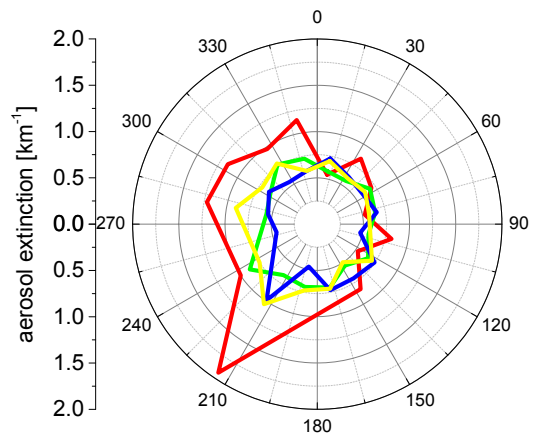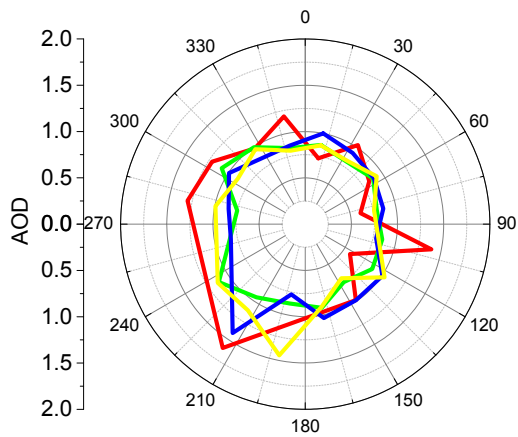
Figure 16: Dependencies of VCDs and AODs (left) and near-surface VMRs and AE (right) of NO$_2$ (a), SO$_2$ (b), HCHO (c) and aerosols (d) on wind direction for individual seasons (different colours).

Tables

Table 1 Settings used for the O_4, NO_2, SO_2 and HCHO DOAS analyses

Parameter	Sources	species			
		O_4	NO_2	SO_2	HCHO
Fitting interval		351-390nm	351-390nm	307.8-330nm	324.6-359nm
Cross section	NO_2: Vandaele et al. (1998), 220 K, 294 K	×	×	× (only 294 K)	× (only 294 K), I_0-corrected[*] (10^{17} molecules/cm^2)
	O_3: Bogumil et al., (2003), 223 K and 243 K	×(only 223 K)	×(only 223 K)	×	× (only 223 K) I_0-corrected[*] (10^{18} molecules/cm^2)
	O_4: Thalman and Volkamer (2013), 293 K	×	×	×	×
	SO_2:Bogumil et al. (2003), 293 K			×	×
	HCHO: Meller and Moortgat (2000), 293 K	×	×	×	×
Ring	Two Ring spectra calculated with DOASIS (Kraus, 2006; Wagner et al., 2009)	×	×	×	×
Polynomial degree		3	3	5	5
Intensity offset		constant	constant	constant	constant

* solar I_0 correction, Aliwell et al., 2002

Table 2 Different filters and corresponding thresholds applied to the retrieved SCDs. Also the corresponding fractions of removed data are shown. (SZA: solar zenith angle; RIO: relative intensity offset; RMS: root mean square of the spectral residual)

O_4 and NO_2		SO_2		HCHO	
filter	percentage	filter	percentage	filter	percentage
SZA < 75°	6.2%	SZA < 75°	5.8%	SZA < 75°	6.1%
RIO < 0.01	5.6%	RIO < 0.01	1.1%	RIO < 0.01	7.1%
RMS < 0.003	0.3%	RMS < 0.01	0.2%	RMS < 0.003	0.2%

5   Table 3 Filter scheme of aerosol and trace gas results derived from MAX-DOAS observations. Filled circles (●): use of measurement is recommended; Open circles (○): use of measurement is not recommended.

	AOD	Aerosol extinction near surface	Profile of aerosol extinction	VCD	VMR near surface	Profile of VMRs
Low aerosol	●	●	●	●	●	●
High aerosol	●	●	●	●	●	●
Cloud holes	○	●	○	●	●	●
Broken clouds	○	●	○	●	●	●
Continuous clouds	○	●	○	●	●	●
fog	○	○	○	○	○	○
Thick clouds	○	○	○	○	○	○

Table 4 Averaged error budget (in %) of the retrieved TG VCDs and AOD, and near-surface (0–200 m) TG VMRs and AE. The total uncertainty is calculated by adding the different error terms in Gaussian error propagation.

	0-200 m				VCD or AOD			
	AE	NO_2	SO_2	HCHO	AOD	NO_2	SO_2	HCHO

Smoothing and noise error	10	12	19	50	6	17	25	50
Algorithm error	4	3	4	4	8	11	10	11
Cross section error	5	3	5	9	5	3	5	9
Related to temperature dependence of cross section	10	2	3	6	10	2	3	6
Related to the aerosol retrieval (only for trace gases)	-	16	16	16	-	15	15	15
Total	16	21	26	54	15	25	31	54

Table 5 Correlation coefficients between hourly averaged trace gas VCDs and AODs (for clear sky conditions) as well as between VMRs and aerosol extinction near the surface (for clear and cloudy conditions except thick clouds and fog). The numbers of the data used for the analyses are given for each season.

	winter		spring		summer		autumn	
	column	surface	column	surface	column	surface	column	surface
Number of observations	375	525	1339	1739	1308	1830	1142	1676
NO_2	0.51	0.69	0.37	0.58	0.48	0.63	0.44	0.65
SO_2	0.52	0.69	0.45	0.62	0.45	0.62	0.44	0.66
HCHO	0.77	0.81	0.51	0.62	0.35	0.62	0.57	0.69